

## Role of flow structures on the deposition of low-inertia particles in turbulent pipe flow

Rasmus Korslund Schlander,<sup>1</sup> Stelios Rigopoulos<sup>1,2</sup> and George Papadakis<sup>1,\*</sup>

<sup>1</sup>*Department of Aeronautics, Imperial College London, London SW7 2AZ, United Kingdom*

<sup>2</sup>*Department of Mechanical Engineering, Imperial College London, London SW7 2AZ, United Kingdom*



(Received 29 May 2023; accepted 18 January 2024; published 20 February 2024)

We analyze the effect of large-scale coherent structures on the deposition of low-inertia particles in a turbulent pipe flow using extended proper orthogonal decomposition (EPOD) and spectral analysis. We perform direct numerical simulations (DNSs) at two the Reynolds numbers 5300 and 10 300 (based on bulk parameters) with the particles released at the pipe inlet. The equilibrium Eulerian model is employed for calculating particle velocity, and the analysis is limited to particles with Stokes number (based on wall units) less than 1. Increasing the Stokes number increases the energy at small streamwise wavelengths (due to inertial clustering), and the spectral energy peak moves from  $\lambda_z^+ \approx 1000$  to  $\lambda_z^+ \approx 150$ . The spectral peak in the  $(\lambda_z^+, y^+)$  plane, where  $y^+$  is the wall-normal distance, moves from the buffer layer to the logarithmic region. Gravity has a substantial effect on the POD mode shapes. For the downward flow, a second peak appears closer to the center. A new Fukagata-Iwamoto-Kasagi (FIK) identity is derived for the wall deposition rate coefficient (Sherwood number,  $Sh$ ) and employed to quantify the contributions of the mean and fluctuating velocity and particle concentration fields for different Stokes, Froude, and Reynolds numbers. Modes with azimuthal wave numbers  $k_\theta$  equal to three or four are found to contribute most to deposition. Application of the developed methodology to higher Reynolds number can elucidate the role of large- and very-large-scale flow structures on particle deposition to the wall. It is well known these structures leave their footprint at the wall but their contribution to deposition is not well understood.

DOI: [10.1103/PhysRevFluids.9.024303](https://doi.org/10.1103/PhysRevFluids.9.024303)

### I. INTRODUCTION

The paper investigates the interaction between low-inertia particles and coherent fluid structures inside a pipe, with the aim to quantify the effect of different structures on particle deposition on the wall. More specifically, we investigate the effect of two parameters, gravity and inertia, at two Reynolds numbers. Understanding the effect of these parameters on particle concentration could lead to better control of deposition in pipes and channels.

Coherent structures in wall-bounded flows have different streamwise and radial extents and four different types have been identified [1]. The first group is near-wall streaks that are located in the viscous and buffer layers and are characterized by alternating high- and low-momentum fluid with a spanwise distance of approximately  $100\nu/u_\tau$ , where  $\nu$  is the kinematic viscosity and  $u_\tau$  is the

\*Corresponding author: [g.papadakis@imperial.ac.uk](mailto:g.papadakis@imperial.ac.uk)

Published by the American Physical Society under the terms of the [Creative Commons Attribution 4.0 International](https://creativecommons.org/licenses/by/4.0/) license. Further distribution of this work must maintain attribution to the author(s) and the published article's title, journal citation, and DOI.

friction velocity [2]. The next group consists of hairpin or horseshoe vortices and is also found in the near-wall and log regions [3]. The last two groups contain large-scale motions (LSMs) and very-large-scale motions (VLSMs), have a presence in the log layer and the outer region of the boundary layer, and a streamwise length from around  $1\delta$  to  $10\delta$ , where  $\delta$  is the outer length scale (in the present case the pipe radius). The VLSMs are centered in the log region but also have a footprint on the wall [4]. For an in-depth review of coherent motions in wall-bounded flows, refer to Refs. [5,6].

Inertial particles in wall-bounded flows and their interaction with the aforementioned coherent structures, especially near-wall streaks, have long been investigated both experimentally and numerically. Inertia prevents particles from completely following the turbulent motion, and this leads to preferential concentration. This was first observed in Squires and Eaton [7]; it is sometimes referred to as the particle centrifuge effect and leads to local areas of very large concentration. In wall-bounded flows, inertial particles are also subject to turbophoresis [8,9], which is the migration of particles from the bulk flow to the wall region. This has been linked to the sweep and ejection events, see Rouson *et al.* [10]. It has been shown that either a particle is re-entrained immediately by the same vortex that carried the particle to the wall, or it stays in the viscous region for a long time [11].

Gravity also affects particle concentration and deposition. Gravitational effects have been investigated numerically using Lagrangian simulations by Uijtewaal *et al.* [12], Marchioli *et al.* [13], and Nilsen *et al.* [14] and experimentally among others by Oliveira *et al.* [15] and Fong *et al.* [16]. The effect of gravity is not easy to quantify because it depends on inertia. In Nilsen *et al.* [14] and Uijtewaal *et al.* [12], an increase in particle concentration in the log region was observed for upward flow, while an increase in concentration in the center was observed for downward flow. More details on particle transport in turbulent flows can be found in the review papers [17,18].

The numerical simulations referred to above track a large number of point particles as they disperse in the turbulent flow; this is known as Lagrangian simulation. For sufficiently low inertia, an alternative is the equilibrium Eulerian particle transport model, originally proposed by Maxey [19], and later extended by Druzhinin [20] and Ferry and Balachandar [21]. The model assumes that the particle velocity at each time instant and spatial location is unique and is in equilibrium with the surrounding fluid velocity. This assumption requires small inertia so that the effect of initial conditions decays exponentially fast. Most importantly, it allows a series expansion of the particle velocity in terms of the Stokes number, a nondimensional parameter that quantifies particle inertia. Substitution of the expansion to the particle motion equation and matching terms of the same order leads to an analytical expression of the particle velocity in terms of the surrounding fluid velocity and its derivatives. This velocity is subsequently employed in the transport equation for particle concentration, therefore providing an entirely Eulerian description of the problem. More details can be found in Refs. [17,21,22].

This approach is numerically more efficient than the Lagrangian approach and can be easily implemented in existing DNS codes. It is accurate provided that the Stokes number based on the Kolmogorov timescale is smaller than 0.2 for homogeneous isotropic turbulence [17,23,24] or 0.6 for homogeneous shear flows [25] and can capture phenomena such as preferential particle concentration and turbophoresis [17]. It has been used in laminar as well as turbulent flows. For example, Pilou *et al.* [26] analyzed the deposition of inertial particles in a  $90^\circ$  pipe bend under laminar flow conditions, Icardi *et al.* [27] simulated polydispersed particles in a turbulent channel flow, Cerminara *et al.* [28] simulated volcanic ash plume using large eddy simulations (LESs), Yang *et al.* [29] studied bubbles in a jet with LESs, Aiyer *et al.* [30] investigated oil droplets in a cross-flow jet, and Balachandar *et al.* [31] suggested this as a method to simulate the airborne transmission of Covid-19 to establish social distancing guidelines.

So far inertial particle dispersion and wall deposition have been investigated mainly with Lagrangian methods. The aforementioned Eulerian equilibrium model offers an alternative perspective and allows the application of a variety of tools that have been developed for passive scalars to low-inertia particles. This in turn can lead to new insights and the discovery of mechanisms that are

not easy to extract using Lagrangian methods. More specifically, in this paper we extract proper orthogonal decomposition (POD) modes of the particle concentration fluctuations and employ extended POD (EPOD) [32] to find the velocity modes most correlated to the concentration modes. EPOD has been used previously to analyze correlated events, such as velocity in two different regions [33], pressure and velocity fluctuations [34], temperature and velocity fluctuations in wall-heated pipes [35], passive scalars in swirling jets [36], etc. To the best of our knowledge, this is the first time POD and EPOD is employed to study particle-laden turbulent flows.

To relate the fluctuating components (and thus flow structures) to particle deposition, an equation similar to the Fukagata-Iwamoto-Kasagi (FIK) identity [37] is also derived. The new equation is valid for low-inertia particles and extends the one derived in Ref. [38] for a passive scalar. The identity is employed to quantify the contribution of individual POD and EPOD modes to the time-average particle deposition rate to the pipe wall. In particular, the coherent structures that have the biggest contribution to  $Sh$  can be identified. Also, it provides closed-form expressions of the effects of particle inertia and gravity on deposition.

The article is structured as follows: the case examined, computational details of the DNS datasets, and a brief overview of POD and EPOD are presented in Sec. II. The FIK identity for low-inertia particles is presented in Sec. III. We analyze the spectra and the POD/EPOD modes in Sec. IV and conclude in Sec. V.

## II. MODELLING DETAILS

### A. Governing equations

We consider the turbulent flow inside a circular pipe with low-inertia particles injected at the inlet. The flow is assumed to be incompressible and the continuity and momentum equations are written in Cartesian tensor notation as

$$\frac{\partial u_i}{\partial x_i} = 0, \quad (1a)$$

$$\frac{\partial u_i}{\partial t} + \frac{\partial u_i u_j}{\partial x_j} = -\frac{\partial p}{\partial x_i} + \frac{1}{\text{Re}} \frac{\partial^2 u_i}{\partial x_j \partial x_j}, \quad (1b)$$

where  $u_i$  is the instantaneous fluid velocity in the  $i$ th direction,  $p$  is the static pressure, and  $t$  is the time. The notation  $\mathbf{x} = (x_1, x_2, x_3)$  for the spatial coordinates is used interchangeably with the notation  $\mathbf{x} = (x, y, z)$ , where  $z = x_3$  is the axial (streamwise) direction. Due to rotational symmetry, it is convenient (especially for data plotting) to use polar coordinates  $(r, \theta, z)$ , where  $(x, y) = (r \cos \theta, r \sin \theta)$ . Velocities are nondimensionalized with the bulk velocity  $U_B$  and distances with the pipe diameter  $D$ . The Reynolds number is defined as  $\text{Re} = U_B D / \nu$ , where  $\nu$  is the kinematic viscosity. The mean, i.e. time-average, and fluctuating quantities are denoted by an overbar and a prime, respectively, for example,  $\bar{u}_i$  and  $u_i'$ .

We assume that the particles have diameters much smaller than the Kolmogorov length scale, the volume fraction is small (so that there are no interparticle collisions and the presence of the particles does not affect the flow), and only the Stokes drag force and gravity act on the particles. Under these conditions, the particles can be considered as discrete points that follow the equation of motion

$$\frac{Dv_i^*}{Dt^*} = \frac{1}{\tau} (u_i^* - v_i^*) + g_i, \quad (2)$$

where  $t^*$  is the dimensional time,  $D/Dt^*$  is the material derivative along the particle trajectory,  $u_i^*$ ,  $v_i^*$ ,  $g_i$  denote the dimensional fluid velocity, particle velocity and gravitational acceleration in the  $i$ th direction, respectively. The particle relaxation time  $\tau$  is defined as

$$\tau = \frac{\rho_p D_p^2}{18\mu_f}, \quad (3)$$

where  $\rho_f$  and  $\mu_f$  are the fluid density and dynamic viscosity, respectively,  $\rho_p$  and  $D_p$  are the particle density and diameter, respectively. In the present simulations, we take  $\rho_p/\rho_f \approx 1000$ . If  $\tau$  is small,  $v_i^*$  can be expanded in a Taylor series as (see Ref. [19])

$$v_i^* = v_i^{(0)} + v_i^{(1)}\tau + \dots \quad (4)$$

Substituting in (2) and equating terms with the same order of  $\tau$ , we get

$$v_i^* = u_i^* - \tau \left( \frac{Du_i^*}{Dt^*} - g_i \right), \quad (5)$$

where only the linear term in the expansion (4) was retained. Extensions of the model to account for other forces in the equation of motion and quadratic terms of  $O(\tau^2)$  can be found in Refs. [19–21]. The model assumes that  $v_i^*(\mathbf{x}, t)$  is unique and is determined solely by the surrounding fluid velocity and its derivatives. The effect of initial conditions is therefore considered to be exponentially decreasing with time; the conditions under which this is satisfied are elaborated in Ref. [21]. Note that (5) implies a continuous particle velocity field,  $v_i^*(\mathbf{x}, t)$ .

We now define the particle concentration  $c^*(\mathbf{x}, t)$  as the volume of particles per unit volume of fluid and assume that this is also a continuous field. The reference quantity for  $c^*(\mathbf{x}, t)$  is the particle concentration at the pipe inlet,  $c_I$ , i.e.,  $c(\mathbf{x}, t) = c^*(\mathbf{x}, t)/c_I$ . The transport equation for  $c(\mathbf{x}, t)$  is

$$\frac{\partial c}{\partial t} + \frac{\partial v_j c}{\partial x_j} = \frac{1}{\text{ReSc}} \frac{\partial^2 c}{\partial x_j \partial x_j}, \quad (6)$$

where Sc is the Schmidt number, defined as  $\text{Sc} = \nu/\Gamma_C$ , where  $\Gamma_C$  is the particle diffusivity. The diffusion coefficient  $\Gamma_C$  due to Brownian motion is much smaller than  $\nu$ , and Sc values range from  $10^2$  to  $10^6$ , see Table 3 of Ref. [39]. Such high values of Sc result in Batchelor scales which are much smaller than the Kolmogorov scale (their ratio scales as  $\text{Sc}^{-0.5}$ ), and are computationally very expensive to resolve. Coarser resolution creates over- and under-shoots in the particle concentration field necessitating the introduction of a total variation diminishing (TVD) scheme in the convection term, or some other form of filtering, such as spectral filtering of high wave numbers as in Refs. [24,40]. To avoid the excessive cost of simulation or the need to employ a filtering scheme, we adopt a compromise approach, where the diffusion term is retained and the Schmidt number is set to  $\text{Sc} = 1$ . In Richter *et al.* [41], Sc was also set to unity, while in the LESs of Yang *et al.* [29] and Aiyer *et al.* [30] molecular diffusion was neglected but an eddy diffusivity model was employed for the subgrid-scale concentration fluxes. Pilou *et al.* [26] investigated particle deposition in a laminar flow and used the diffusion coefficient due to Brownian motion. For a laminar flow, this is the correct approach because there is no other mechanism to diffuse particle concentration. For a turbulent flow however, diffusion due to turbulence [represented by the second term in equation (6)] is expected to be dominant and this term is well resolved with the current grid (see computational details below). The problem with the Sc number is well known and appears in many other areas. For example, in turbulent reacting flows in liquids the true Sc is very high, but values close to one are also used for the viscous terms of the reactants to make the simulations tractable, see Ref. [42].

Inserting the nondimensional form of (5) into (6), we obtain

$$\frac{\partial c}{\partial t} + \frac{\partial}{\partial x_j} \left\{ \left[ u_j + \text{St} \left( \frac{1}{\text{Fr}_j} - \frac{\partial u_j}{\partial t} - u_k \frac{\partial u_j}{\partial x_k} \right) \right] c \right\} = \frac{1}{\text{ReSc}} \frac{\partial^2 c}{\partial x_j \partial x_j}, \quad (7)$$

where  $\text{Fr}_i = U_B^2/g_i D$  and  $\text{St} = \tau U_B/D$  are the Froude and Stokes numbers, respectively (based on global variables). When  $\text{Fr}_z > 0$ , gravity is aligned with the mean streamwise velocity, corresponding to downward flow in a vertical pipe. Similarly, when  $\text{Fr}_z < 0$  the flow is moving upwards in a vertical pipe.

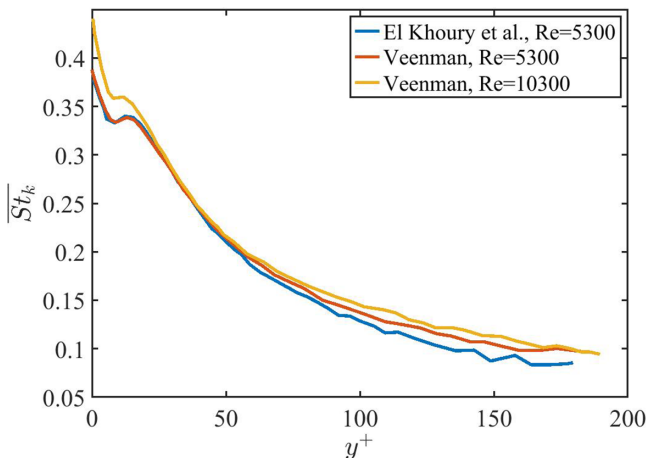


FIG. 1. Variation of  $\overline{St}_k$  (based on the Kolmogorov timescale  $\tau_k$ ) in the wall-normal direction. The dissipation rate used to calculate  $\tau_k$  is taken from Refs. [43,44].

### B. Computational details

We perform DNS of a fully developed turbulent flow in a pipe of length  $L = 7.5D$ . Two Reynolds numbers are considered,  $Re = 5300$  and  $10\,300$ . The flow is driven by a constant streamwise pressure gradient. For velocities, periodic boundary conditions are employed at the inlet and outlet planes, while a no-slip condition is imposed at the wall.

Three Stokes numbers are defined. The first is based on wall values,  $St^+ = \tau u_\tau^2 / \nu$ , where  $u_\tau$  is the friction velocity (we take  $St^+ = 1.0$  for both Reynolds numbers). The second is based on bulk values,  $St = \tau U_B / D$ , and is equal to  $0.04$  for  $Re = 5300$  and  $0.026$  for  $Re = 10\,300$ . Finally, we define  $St_k = \tau / \tau_k$ , where  $\tau_k$  is the Kolmogorov timescale. The value of  $\overline{St}_k$  (based on the time-, streamwise- and azimuthally averaged dissipation) changes along the radius, see Fig. 1. It can be seen that the maximum is approximately  $0.4$  for  $Re = 5300$  and  $0.45$  for  $Re = 10\,300$ . These values are located at the wall, where the dissipation rate is maximized, and the Kolmogorov timescale  $\tau_k$  is minimized. The minimum  $St_k$  value is approximately  $0.1$  for both Reynolds numbers and located at the center of the pipe. For Froude number three cases are considered,  $1/Fr_z = 0$  (no gravity effect) and  $Fr_z = \pm 0.4$  (upward or downward flow in a vertical pipe).

The particles are inserted at the inlet of the pipe with uniform concentration  $c^*(r, \theta, 0) = c_I$ . Since we are interested in particle deposition, we assume a totally absorbing wall with  $c(R, \theta, z) = 0$ . This boundary condition is known as a perfect sink model; particles are irreversibly absorbed at the wall upon impact [45]. At the exit plane, a nonreflecting boundary condition is employed,  $\partial c / \partial t + \partial v_z c / \partial z = 0$ , where  $v_z(r, \theta, L)$  is the local instantaneous axial particle velocity.

The governing equations are solved using an in-house unstructured finite-volume solver Pantarhei [46–49]. The convection and diffusion terms are discretized using a second-order central approximation. A third-order backward difference scheme is employed for the transient term. Orthogonal diffusion terms are treated implicitly, while the convection and non-orthogonal diffusion terms are treated explicitly using third-order extrapolation in time. The fractional step method is employed to correct velocities and pressure to satisfy the continuity equation at the end of each time step. The resulting linear systems are solved with the generalized minimal residual method (GMRES) iterative algorithm implemented in the PETSc library [50]. Convergence is accelerated using an algebraic multigrid preconditioner from the Hypr library [51].

The grid near the center is H type and transitions to O type closer to the wall to fit the cylindrical boundary. The computational domain spans  $7.5D$ , large enough to resolve the largest coherent structures according to Wu *et al.* [52], and the particles are reinserted from the outlet

TABLE I. Parameter settings for the simulations.

Re	$Re_\tau$	$N_c$	$\Delta r_{\text{wall}}^+$	$\Delta \theta r_{\text{max}}^+$	$\Delta r_{\text{center,max}}^+$	$\Delta z^+$	$\Delta t [\frac{R}{U_B}]$	$N_t$
5300	180	$8.8 \times 10^6$	0.35	3.75	2.29	5.25	0.008	600
10 300	323	$25.6 \times 10^6$	0.1	4.84	2.63	8.2	0.004	600

to the inlet to artificially increase the length from  $7.5D$  to  $15D$  to ensure that the normalized concentration profiles become self-similar (see more details on this below). For  $Re = 5300$ , the cross section is discretized with  $N_{c,\text{cross}} = 1.7 \times 10^4$  cells and  $N_z = 512$  layers are employed in the streamwise direction, resulting in a total of  $N_c = 8.8 \times 10^6$  cells (for  $Re = 10\,300$  we use  $25.6 \times 10^6$  cells). Grid spacings (in wall units) in the radial, azimuthal and axial directions are provided in Table I. The ratio of the local grid size (computed as the cubic root of the cell volume) to the Kolmogorov length scale  $\eta = (v^3/\epsilon)^{0.25}$ , where  $\epsilon$  is the average dissipation rate, is less than 1.8 in most parts of the domain, which indicates that the flow is well resolved [53]. The time steps are  $\Delta t = 0.008R/U_B$  and  $\Delta t = 0.004R/U_B$  for  $Re = 5300$  and  $10\,300$ , respectively, corresponding to a maximum Courant–Friedrichs–Lewy number of 0.6. Statistics were collected over 20 000 time steps, corresponding to  $160R/U_B$ . In total 600 velocity and particle concentration snapshots are stored every  $250\Delta t$  (corresponding to  $\Delta t_s = 2R/U_B$  for the lowest  $Re$  number) and processed to extract POD and EPOD modes. More details and validation against reference data for  $Re = 5300$  can be found in Schlander *et al.* [38].

To validate the equilibrium Eulerian model, we perform additional DNS simulations in a channel flow at  $Re_\tau = 180$  (same as in the pipe flow for the case of  $Re = 5300$ ) and compare the particle velocity field against the Lagrangian simulations of Ref. [22]. The channel has dimensions  $(L_x, L_y, L_z) = (4\pi, 2, 4/3\pi)$  and the domain is discretized with  $(N_x, N_y, N_z) = (256, 128, 256)$  cells in each direction (9.3 million cells in total). Using equation (5), the following expressions are obtained for the streamwise and wall-normal particle velocities for channel flow,

$$\bar{v}_y = -St \frac{\partial \overline{u_y'^2}}{\partial y}, \quad (8)$$

$$\bar{v}_x = \bar{u}_x - St \frac{\partial \overline{u_x' u_y'}}{\partial y}. \quad (9)$$

As shown in Fig. 2(a), the mean wall-normal particle velocity for  $St^+ = 1$  and  $St^+ = 3$  matches very well with the Lagrangian simulation results reported in Ref. [22]. However, for the streamwise fluid and particle velocity difference, shown in Fig. 2(b), the agreement is good for  $St^+ = 1$ , but there are deviations (especially around the minimum value) for  $St^+ = 3$ . This is in agreement with the results of Ref. [40], where instantaneous particle concentration histograms using the Eulerian model match well with Lagrangian simulations for  $St^+ = 1$  [see Fig. 6(b) of Ref. [40]]. Based on the above results, we conclude that the equilibrium Eulerian model is sufficiently accurate for  $St^+ = 1$  (at least for the geometry and conditions examined in this paper) and in the following sections we restrict our investigations to  $St^+ \leq 1$ .

### C. Proper and extended proper orthogonal decomposition (POD and EPOD)

POD is a modal technique that decomposes a fluctuating field in terms of modes ranked according to their energy [54]. Below we give a brief description of POD and EPOD modes; for more details see Schlander *et al.* [38]. In particular, refer to Appendix A of Ref. [38] for the weighting matrix that is used to define the inner product in the vector space that consists of the three velocity components and the scalar.

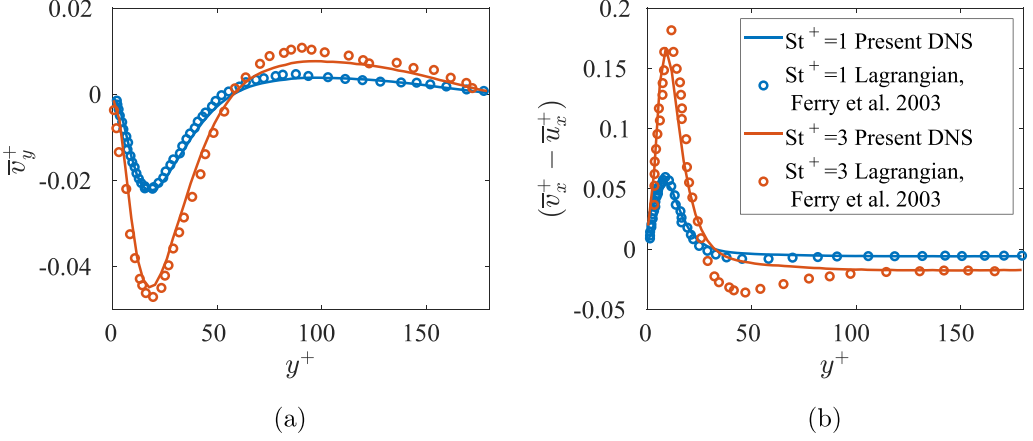


FIG. 2. (a) Wall-normal particle velocity and (b) the difference between the average streamwise particle and fluid velocities for channel flow at  $Re_\tau = 180$ ; profiles are compared with the Lagrangian simulation results of Ferry *et al.* [22]. Solid lines denote the present DNS and  $\circ$  the Lagrangian simulations. The blue line denotes  $St^+ = 1$  and the red line  $St^+ = 3$ .

We define the normalized particle concentration  $c_h(r, \theta, z, t)$  as

$$c_h(r, \theta, z, t) = \frac{\bar{c}_w - c(r, \theta, z, t)}{\bar{c}_w - \bar{c}_B(z)} = \frac{c(r, \theta, z, t)}{\bar{c}_B(z)}, \quad (10)$$

because  $c_w = \bar{c}_w = 0$  and  $\bar{c}_B(z)$  is the bulk concentration, defined as  $\bar{c}_B(z) = 8 \int_0^{1/2} \bar{u}_z \bar{c} r dr$ . As will be shown later in Fig. 3, for  $z > 10D$ , the time average  $\bar{c}_h(r, \theta, z)$  is independent of  $z$ , thus  $z$  becomes a homogeneous direction (this is denoted by the subscript  $h$  in  $c_h$ ). We apply POD on a section of the dataset, from  $z = 10D$  to  $15D$ , where  $c_h$  is homogeneous.

In homogeneous directions, the POD modes reduce to sinusoidal (Fourier) modes. Therefore, the fluctuating velocity and normalized particle concentration fields, denoted by the generic variable  $\mathbf{q}(r, \theta, z, t)$  below, can be Fourier transformed in the azimuthal and streamwise directions as

$$\mathbf{q}(r, \theta, z, t) = \sum_{k_z=-\infty}^{+\infty} \sum_{k_\theta=-\infty}^{+\infty} \hat{\mathbf{q}}_{k_\theta, k_z}(r, t) e^{i(k_\theta \theta + 2\pi k_z \frac{z}{L})}, \quad (11)$$

where  $\hat{\mathbf{q}}_{k_\theta, k_\theta}(r, t)$  is the Fourier coefficient,  $k_z$  is the streamwise wave number, and  $k_\theta$  is the azimuthal wave number. The Fourier coefficients are stacked column-wise in one snapshot matrix for each wave number pair,

$$\hat{\mathbf{Q}}_{k_\theta, k_z} = [\hat{\mathbf{q}}_{k_\theta, k_z}^{(1)}, \hat{\mathbf{q}}_{k_\theta, k_z}^{(2)}, \dots, \hat{\mathbf{q}}_{k_\theta, k_z}^{(N_t)}], \quad (12)$$

where  $N_t$  is the total number of snapshots. We then solve the eigenvalue problem of size  $N_t$ ,

$$\frac{1}{N_t} \hat{\mathbf{Q}}_{k_\theta, k_z}^* \mathbf{W} \hat{\mathbf{Q}}_{k_\theta, k_z} \Psi_{k_\theta, k_z} = \Psi_{k_\theta, k_z} \Lambda_{k_\theta, k_z}, \quad (13)$$

where  $\Psi_{k_\theta, k_z}$  is the temporal eigenvector,  $\Lambda_{k_\theta, k_z} = \text{diag}[\lambda_{k_\theta, k_z}^{(1)}, \lambda_{k_\theta, k_z}^{(2)}, \dots, \lambda_{k_\theta, k_z}^{(N_t)}]$  is a diagonal matrix containing the eigenvalues (by convention  $\lambda_{k_\theta, k_z}^{(1)} \geq \lambda_{k_\theta, k_z}^{(2)} \geq \dots \geq \lambda_{k_\theta, k_z}^{(N_t)}$ ) and  $\mathbf{W}$  is a weighting matrix that accounts for the area expansion in the radial direction. The spatial modes can be recovered from

$$\Phi_{k_\theta, k_z} = \frac{1}{\sqrt{N_t}} \hat{\mathbf{Q}}_{k_\theta, k_z} \Psi_{k_\theta, k_z} \Lambda_{k_\theta, k_z}^{-1/2}, \quad (14)$$

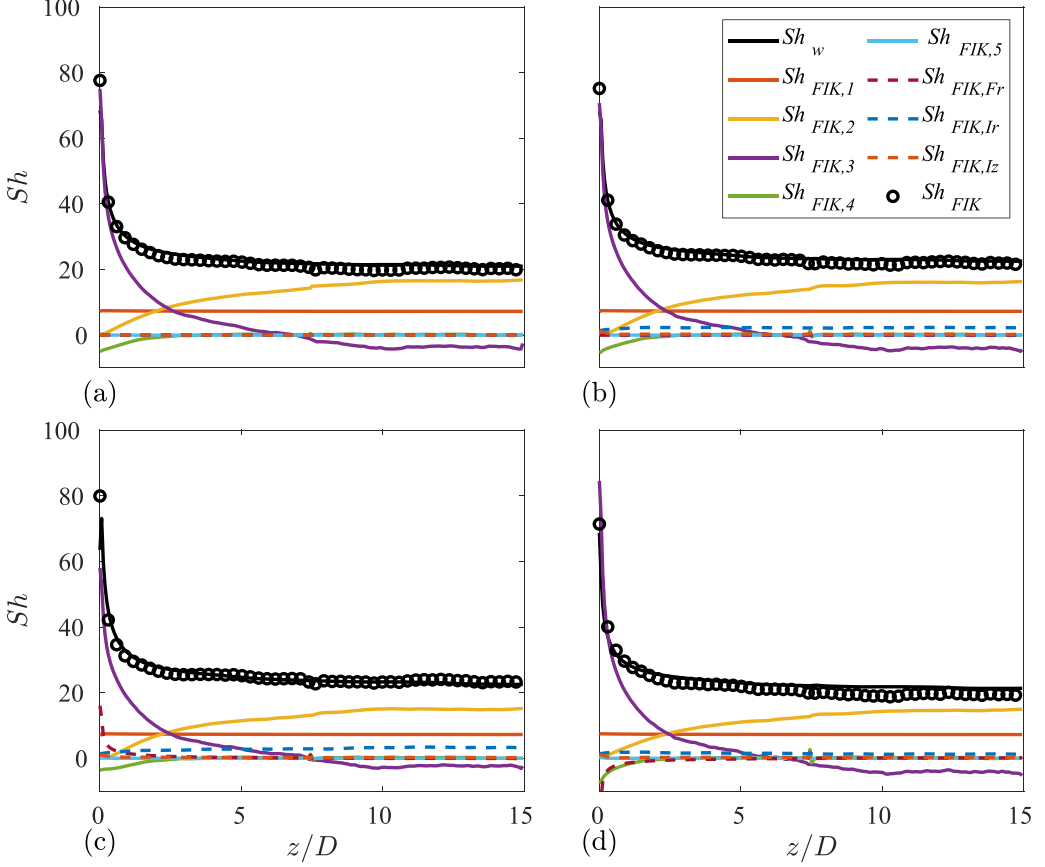


FIG. 3. Variation of  $Sh$  number and the constituent components  $Sh_{\text{FIK}}$  along the length of the pipe for  $Re = 5300$ , where panel (a) is for  $St^+ = 0$ , panel (b) is for  $St^+ = 1$ ,  $1/Fr_z = 0$ , panel (c) is for  $St^+ = 1$ ,  $Fr_z = 0.4$ , and panel (d) is for  $St^+ = 1$ ,  $Fr_z = -0.4$ .

where  $\Phi_{k_\theta, k_z} = [\phi_{k_\theta, k_z}^{(1)}, \phi_{k_\theta, k_z}^{(2)}, \dots, \phi_{k_\theta, k_z}^{(N_t)}]$ . The last factor,  $\Lambda_{k_\theta, k_z}^{-1/2}$ , ensures that the modes  $\phi_{k_\theta, k_z}^{(n)}$  are orthonormal. Keeping only the  $k \ll N_t$  largest eigenvalues, an approximate reconstruction of the flow or particle concentration fields can be obtained from

$$\hat{\mathbf{Q}}_{k_\theta, k_z}^{(k)} = \sqrt{N_t} \Phi_{k_\theta, k_z}^{(\leq k)} \Lambda_{k_\theta, k_z}^{(\leq k)1/2} \Psi_{k_\theta, k_z}^{(\leq k)*}, \quad (15)$$

where the superscript  $(\leq k)$  denotes the truncated version of the corresponding matrices, for example,  $\Phi_{k_\theta, k_z}^{(\leq k)} = [\phi_{k_\theta, k_z}^{(1)}, \phi_{k_\theta, k_z}^{(2)}, \dots, \phi_{k_\theta, k_z}^{(k)}]$  and  $\Lambda_{k_\theta, k_z}^{(\leq k)} = \text{diag}[\lambda_{k_\theta, k_z}^{(1)}, \lambda_{k_\theta, k_z}^{(2)}, \dots, \lambda_{k_\theta, k_z}^{(k)}]$ .

The extended POD (EPOD), introduced by Maurell *et al.* [33] and Boree [32], is employed to analyze correlations between different variables. The temporal basis,  $\Psi_{k_\theta, k_z}$ , obtained from the standard POD of one variable, is used to find the spatial modes of another synchronized variable. Here we aim to investigate the correlation between velocity and particle concentration fluctuations. Therefore, the temporal basis obtained from the POD analysis of the particle concentration fluctuations will be used to decompose the velocity field. The velocity EPOD modes are obtained from:

$$\Phi_{k_\theta, k_z, e} = \frac{1}{\sqrt{N_t}} \hat{\mathbf{Q}}_{k_\theta, k_z, v} \Psi_{k_\theta, k_z, s} \Lambda_{k_\theta, k_z, s}^{-1/2}, \quad (16)$$

where  $\Phi_{k_\theta, k_z, e} = [\phi_{k_\theta, k_z, e}^{(1)}, \phi_{k_\theta, k_z, e}^{(2)}, \dots, \phi_{k_\theta, k_z, e}^{(N_i)}]$  is the matrix containing the EPOD modes (the subscript  $e$  stands for extended),  $\hat{\mathbf{Q}}_{k_\theta, k_z, v}$  is the snapshot matrix containing the Fourier-transformed velocities (as indicated by the subscript  $v$ ), and  $\Psi_{k_\theta, k_z, s}$  is the temporal mode of the particle concentration field (indicated by the subscript  $s$ ). The kinetic energy associated with each EPOD velocity mode is stored in the diagonal matrix,

$$\Lambda_{k_\theta, k_z, e} = \Lambda_{k_\theta, k_z, s} \Phi_{k_\theta, k_z, e} \Phi_{k_\theta, k_z, e}^* \mathbf{W}, \quad (17)$$

see Boree [32]. The energy contained in each EPOD mode will be lower compared with the standard velocity POD mode because the extended modes are no longer ranked based on their kinetic energy. The reconstruction of the velocity field using the  $k$ -largest EPOD modes is obtained from

$$\hat{\mathbf{Q}}_{k_\theta, k_z, e}^{(k)} = \sqrt{N_t} \Phi_{k_\theta, k_z, e}^{(\leq k)} \Lambda_{k_\theta, k_z, s}^{(\leq k)1/2} \Psi_{k_\theta, k_z, s}^{(\leq k)*}, \quad (18)$$

where we have retained the notation of (15). Here, by largest EPOD modes, we mean the EPOD modes with the largest associated POD scalar variance.

### III. FIK IDENTITY FOR WALL DEPOSITION OF LOW-INERTIA PARTICLES

The FIK identity was first derived by Fukagata *et al.* [37] for the skin friction coefficient for channel, pipe, and flat plate boundary layer flows. In the present paper, we follow the same steps to derive an expression for the wall deposition of low-inertia particles, which is quantified by the nondimensional Sherwood number,

$$\text{Sh} = - \frac{1}{(\bar{c}_B - \bar{c}_W)} \frac{\partial \bar{c}}{\partial r} \Big|_{r=1}, \quad (19)$$

where  $\bar{c}_W$  is the concentration at the wall (in our case  $\bar{c}_W = 0$ ). For the derivation of the FIK identity for the Sh number, we first write the particle concentration equation (6) in polar coordinates, take the time average, assume rotational symmetry and integrate over the cross section of the pipe (the full derivation can be found in Appendix). The resulting expression can be written as a sum of a noninertial component (valid for passive scalars with  $\text{St} = 0$ ) and an inertial component,

$$\text{Sh} = \text{Sh}_{\text{passive}} + \text{Sh}_{\text{inertial}}. \quad (20)$$

The noninertial component was derived in Schlander *et al.* [38]:

$$\begin{aligned} \text{Sh}_{\text{passive}} = & \underbrace{-\frac{8}{(\bar{c}_B - \bar{c}_W)} \int_0^1 r^2 \frac{\partial \bar{c}}{\partial r} dr}_{\text{Sh}_{\text{FIK},1}} + \underbrace{\frac{8\text{ReSc}}{(\bar{c}_B - \bar{c}_W)} \int_0^1 r^2 \overline{u'_r c'} dr}_{\text{Sh}_{\text{FIK},2}} + \underbrace{\frac{4\text{ReSc}}{(\bar{c}_B - \bar{c}_W)} \int_0^1 r(1-r^2) \left\langle \frac{\partial \overline{u_z \bar{c}}}{\partial z} \right\rangle dr}_{\text{Sh}_{\text{FIK},3}} \\ & + \underbrace{\frac{4\text{ReSc}}{(\bar{c}_B - \bar{c}_W)} \int_0^1 r(1-r^2) \left\langle \frac{\partial \overline{u'_z c'}}{\partial z} \right\rangle dr}_{\text{Sh}_{\text{FIK},4}} - \underbrace{\frac{4}{(\bar{c}_B - \bar{c}_W)} \int_0^1 r(1-r^2) \left\langle \frac{\partial^2 \bar{c}}{\partial z^2} \right\rangle dr}_{\text{Sh}_{\text{FIK},5}}. \end{aligned} \quad (21)$$

The inertial component, which applies only to particles, takes the form

$$\begin{aligned} \text{Sh}_{\text{inertial}} = & \underbrace{\frac{8\text{StReSc}}{(\bar{c}_B - \bar{c}_W)} \int_0^1 r^2 \bar{I}_r dr}_{\text{Sh}_{\text{FIK},I_r}} + \underbrace{\frac{4\text{StReSc}}{(\bar{c}_B - \bar{c}_W)} \int_0^1 r(1-r^2) \frac{1}{\text{Fr}_z} \left\langle \frac{\partial \bar{c}}{\partial z} \right\rangle dr}_{\text{Sh}_{\text{FIK},\text{Fr}}} \\ & + \underbrace{\frac{4\text{StReSc}}{(\bar{c}_B - \bar{c}_W)} \int_0^1 r(1-r^2) \langle \bar{I}_z \rangle dr}_{\text{Sh}_{\text{FIK},I_z}}, \end{aligned} \quad (22)$$

where  $\bar{I}_r$  contains the terms arising from  $v_r$ ,  $\bar{I}_z$  the terms arising from  $v_z$ , and  $\text{Fr}_z$  accounts for the effect of streamwise gravity. The expressions for  $\bar{I}_r$  and  $\bar{I}_z$  can be found in Appendix. Angular brackets  $\langle \cdot \rangle$  indicate the operation

$$\langle f \rangle = f - 2 \int_0^1 f r dr, \quad (23)$$

where  $f$  is a generic variable. Note that for equations (21) and (22), the reference quantities for distance and velocity are the pipe radius  $R$  and twice the bulk velocity  $2U_B$  (instead of  $D$  and  $U_B$ , respectively). This is done in order to facilitate the derivation and simplify the form of the FIK identity.

We later show that  $\bar{I}_z$  is negligible in the entire domain. The nonzero terms in  $\text{Sh}_{\text{FIK},I_r}$  are found to be

$$\begin{aligned} \text{Sh}_{\text{FIK},I_r} &\approx \underbrace{-\frac{8\text{StReSc}}{(\bar{c}_B - \bar{c}_W)} \int_0^1 r^2 \bar{c} \frac{\partial \bar{u}_r^2}{\partial r} dr}_{\text{Sh}_{\text{FIK},I_r1}} - \underbrace{\frac{8\text{StReSc}}{(\bar{c}_B - \bar{c}_W)} \int_0^1 r^2 \bar{c} \frac{\bar{u}_r^2 - \bar{u}_\theta^2}{r} dr}_{\text{Sh}_{\text{FIK},I_r2}} - \underbrace{\frac{8\text{StReSc}}{(\bar{c}_B - \bar{c}_W)} \int_0^1 r^2 c' \frac{D\bar{u}_r}{Dt} dr}_{\text{Sh}_{\text{FIK},I_r3}}. \end{aligned} \quad (24)$$

The first two terms represent the effect of turbophoresis, a mechanism whereby inertia causes a drift against the gradient of turbulent kinetic energy, see Reeks [9]. The third term represents correlations between particle concentration fluctuations and radial acceleration and was analyzed by Richter *et al.* [41].

The Sherwood number can be obtained directly from the wall gradient and is shown with a black line in Fig. 3. The maximum value of  $\text{Sh}$  is found close to the inlet, where the boundary layer of particle concentration is very thin (recall that the distribution is uniform at the inlet). For  $z > 10D$ ,  $\text{Sh}$  is approximately constant (and equal to 20.5 at the exit); this indicates that the ratio  $\bar{c}_h(r, \theta, z) = \bar{c}(r, \theta, z)/\bar{c}_W(z)$  does not vary in the streamwise direction, thus  $z$  becomes a homogeneous direction justifying the Fourier transform (11). In Ref. [55] particles with  $\text{St}^+ = 1$  require a longer distance, approximately  $25D$ , to reach equilibrium; similar results are reported in Ref. [56]. However, in both papers, the particles were released close to the center of the pipe and this results in a longer development length.

The different terms on the right-hand side of equations (21) and (22) are shown with colored solid lines in Fig. 3 for  $\text{Re} = 5300$ . To validate the FIK identity, the sum of the right-hand side of equation (20) is plotted as circles, and matches DNS with a level of accuracy similar to Refs. [57–59].  $\text{Sh}_{\text{FIK},1}$  is the contribution from the mean field, see Ref. [38] for discussion about this term. The turbulent flux term,  $\text{Sh}_{\text{FIK},2}$ , grows steadily and attains a maximum value at  $10D$ , where it stabilizes. Close to the inlet,  $\text{Sh}_{\text{FIK},3}$  is large and positive, but it quickly decays and stabilizes to a negative value for  $z > 10D$ . This was also observed for the Nusselt number FIK identity in Ref. [58]. Note that  $\text{Sh}_{\text{FIK},3}$  would have decreased to zero, if we had normalized  $\bar{c}^*(z)$  with the bulk concentration  $\bar{c}_B(z)$ , instead of the inlet value,  $c_I$ . Terms  $\text{Sh}_{\text{FIK},4}$  and  $\text{Sh}_{\text{FIK},5}$  are negligible in the whole domain, apart from the inlet. For larger  $\text{Re}$ , the contribution of  $\text{Sh}_{\text{FIK},2}$  is expected to increase; this will be shown in the next section. The inertial term,  $\text{Sh}_{\text{FIK},\text{Fr}}$ , is negligible except near the inlet, and  $\text{Sh}_{\text{FIK},I_z}$  is negligible in the whole domain.

At the outlet  $\text{Sh} \approx \text{Sh}_{\text{FIK},1} + \text{Sh}_{\text{FIK},2} + \text{Sh}_{\text{FIK},3} + \text{Sh}_{\text{FIK},I_r}$ . For  $\text{St}^+ = 1$ , the radial inertial term  $\text{Sh}_{\text{FIK},I_r} \approx 2$  for  $1/\text{Fr}_z = 0$  (i.e., no gravity),  $\text{Sh}_{\text{FIK},I_r} \approx 4$  for  $\text{Fr}_z = 0.4$ , and  $\text{Sh}_{\text{FIK},I_r} \approx 1$  for  $\text{Fr}_z = -0.4$ . Thus  $\text{Sh}_{\text{FIK},I_r}$  accounts for between 5% and 20% of the total  $\text{Sh}$ , depending on gravity.

We now analyze the effect of Reynolds number on particle deposition. The Sherwood number plot along the streamwise direction for  $\text{Re} = 10\,300$  is qualitatively very similar to Fig. 3, so it is omitted here for brevity. Instead, in Fig. 4 bar charts are shown with the contributions of the nonzero components of equation (21) at the pipe outlet for  $\text{Re} = 5300$  and  $10\,300$ . Absolute and normalized

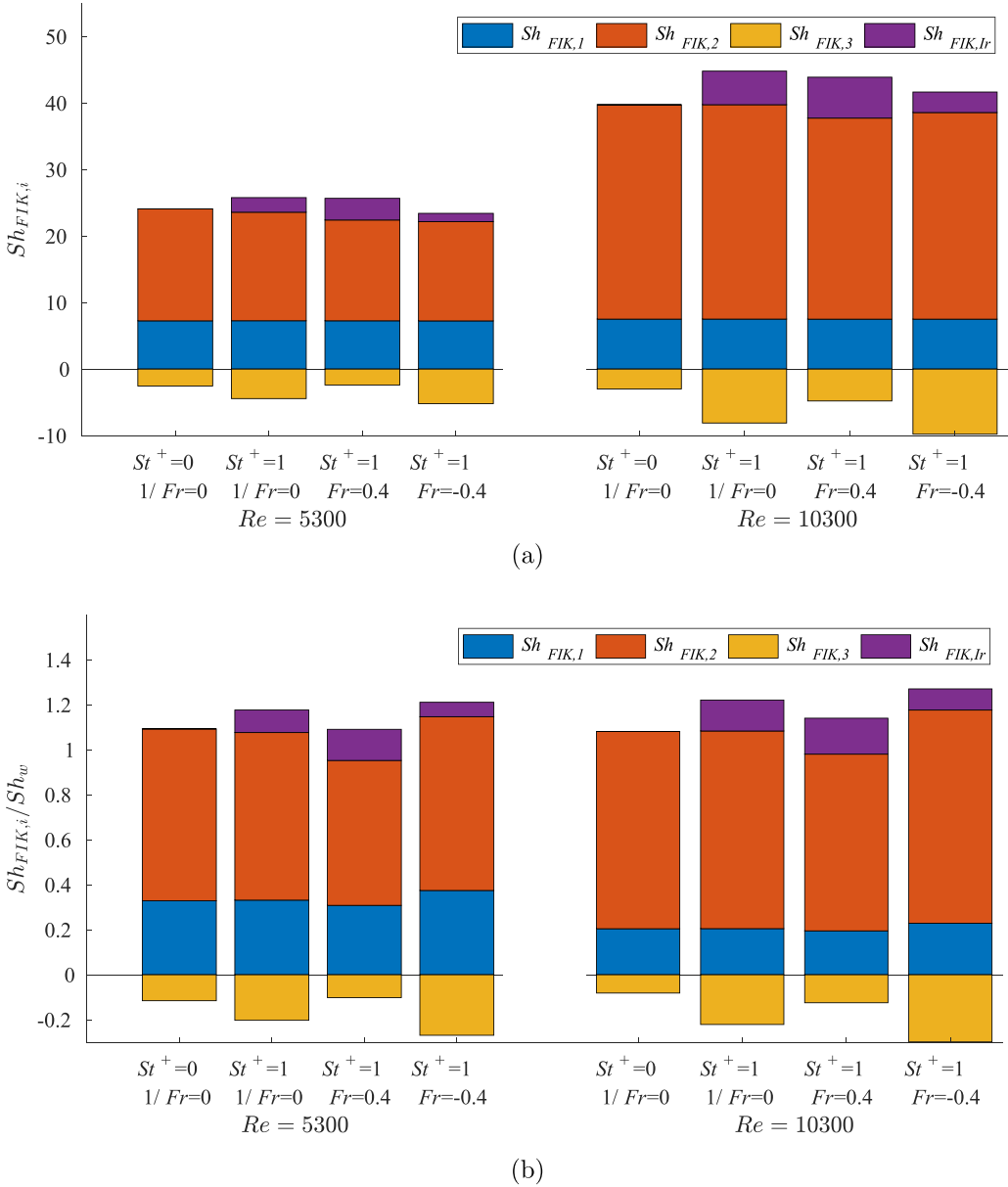


FIG. 4. Bar charts of the nonzero FIK components at  $z = 15D$  for  $Re = 5300$  and  $Re = 10300$ . (a) Absolute values and (b) values normalized with  $Sh$ .

(with  $Sh$ ) values are shown at the top and bottom panels, respectively. The normalized contribution of  $Sh_{FIK,1}$  [see Fig. 4(b)] is reduced significantly for the larger Reynolds number; this is expected as  $Sh_{FIK,1}$  corresponds to the laminar contribution. This term is slightly affected by the flow direction (effect of gravity). The inertial term  $Sh_{FIK,Ir}$  increases with Reynolds number, the increase is largest for the positive Froude number (downward flow), but the effect is rather small. The absolute value of  $Sh$  increases significantly with  $Re$  [see Fig. 4(a)] and the largest contribution arises from  $Sh_{FIK,2}$ , as expected. The effect of inertial terms is more noticeable at the highest  $Re$ , especially for the no-gravity and downward flow cases.

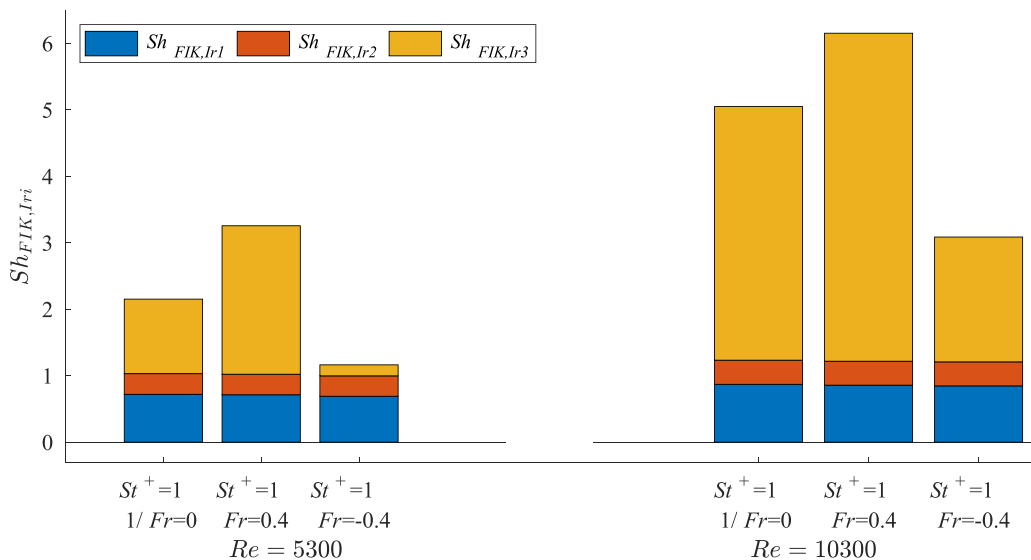


FIG. 5. Bar charts of the absolute values of the nonzero inertial FIK components at  $z = 15D$  for  $Re = 5300$  and  $Re = 10300$ .

A bar chart of the components of the  $Sh_{\text{FIK},\text{Ir}}$  term is shown in Fig. 5. The turbophoresis terms  $Sh_{\text{FIK},\text{Ir}1}$  and  $Sh_{\text{FIK},\text{Ir}2}$  are almost independent of gravity. The  $Sh_{\text{FIK},\text{Ir}3}$  term increases significantly with  $Re$  (it becomes the dominant term for  $Re = 10300$ ) and is also the one that is primarily affected by gravity.

## IV. RESULTS

### A. Spectra

We now analyze the spectra of the particle concentration fluctuations. In Fig. 6 contours of the premultiplied spectra  $k_z k_\theta E_{c_i, c_h}$  are shown in the wavelength plane ( $\lambda_z^+$ ,  $\lambda_\theta^+$ ) at  $y^+ = 15$  for  $St^+ = 0$  and  $St^+ = 1$ . A log scale in both axes together with premultiplied spectra allows us to identify the wavelengths that carry most of the energy (variance in the present case). Such plots are more difficult to obtain with Lagrangian simulations because of the sensitivity to the bin size when computing Eulerian statistics from discrete particle positions, see Ref. [56] for details.

The effect of Stokes number is to increase the energy of the low wavelengths, see top-row Figs. 6(a) and 6(b) where gravity omitted,  $1/Fr_z = 0$ . This is due to inertial clustering. A contour plot of concentration for two Stokes numbers is shown in Fig. 7. For  $St^+ = 1$  localized patches of a high concentration of particles as well as regions almost void of particles can be clearly seen. These localized regions result in the shift of the spectra to lower wavelengths. This amplification of smaller wavelengths was also observed in the one-dimensional spectra of the Lagrangian particle simulation in Ref. [60]. The mechanism for particle clustering was explained by Maxey [19] and it is due to the nonzero divergence of the particle velocity field,  $\nabla \cdot \mathbf{v} \neq 0$ . Using the (nondimensional form) of equation (5) and taking into account that  $\nabla \cdot \mathbf{u} = 0$ , we have

$$\nabla \cdot \mathbf{v} = -St \frac{\partial u_j}{\partial x_i} \frac{\partial u_i}{\partial x_j} = -\frac{St}{4} \left[ \left( \frac{\partial u_i}{\partial x_j} + \frac{\partial u_j}{\partial x_i} \right)^2 - \left( \frac{\partial u_i}{\partial x_j} - \frac{\partial u_j}{\partial x_i} \right)^2 \right] = -St(\|\mathbf{S}\|^2 - \|\mathbf{\Omega}\|^2), \quad (25)$$

where  $\|\mathbf{S}\|^2 = S_{ij}S_{ij}$  and  $\|\mathbf{\Omega}\|^2 = \Omega_{ij}\Omega_{ij}$  are the Frobenius norms of the strain-rate  $\mathbf{S}$  and rotation-rate  $\mathbf{\Omega}$  tensors, respectively. From equation (25), it can be seen that particles will cluster ( $\nabla \cdot \mathbf{v} < 0$ )

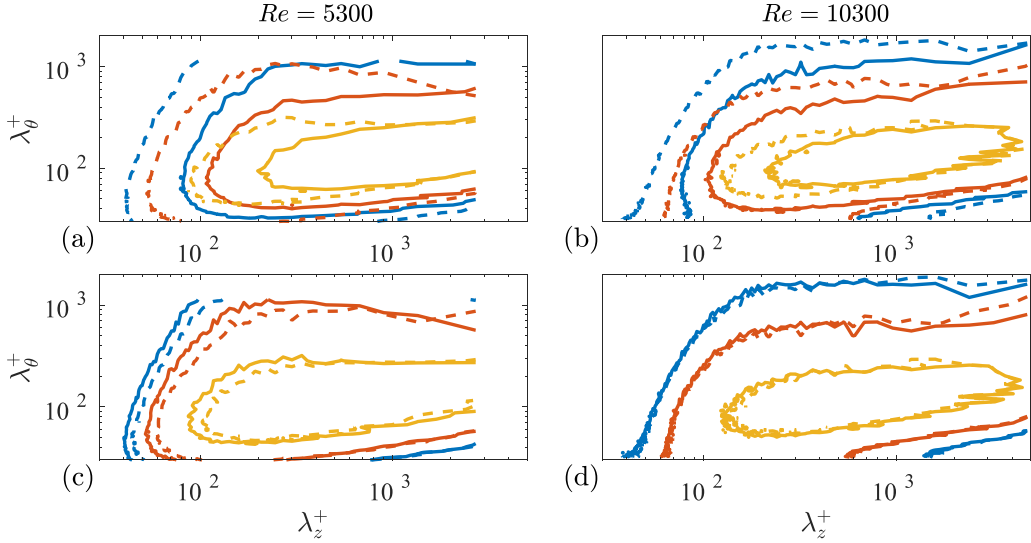


FIG. 6. Premultiplied spectra of particle concentration for (a), (c)  $Re = 5300$  and (b), (d)  $Re = 10300$  at  $y^+ = 15$  for (a), (b) no-gravity flow, and (c), (d) downward flow or upward flow. The blue line marks 10%, the red line 50%, and the yellow line 75% of the maximum value. In panels (a) and (b) the solid line denotes  $St^+ = 0$  (passive scalar) and the dashed line  $St^+ = 1$ . In panels (c) and (d) the Stokes number is constant ( $St^+ = 1$ ), the solid line denotes the downward flow and the dashed line the upward flow.

in areas where the strain rate dominates the rotation rate, for example, at the edge of vortices, see Ref. [61].

The peak of the spectra shifts from  $\lambda_z^+ \approx 1000$ ,  $\lambda_\theta^+ \approx 100$ , which are the well-known spacings of near-wall streaks, to around  $\lambda_z^+ \approx 600$ ,  $\lambda_\theta^+ \approx 100$ . The effect of the Stokes number is the same for both Reynolds numbers, namely, smaller wavelengths are amplified, but it is more pronounced in the low Reynolds number spectra, where the shift to smaller wavelengths is more pronounced.

In Figs. 6(c) and 6(d) the spectra at  $y^+ = 15$  are plotted for  $Fr_z = \pm 0.4$  and  $St^+ = 1$ . For the downward flow ( $Fr_z > 0$ ), the smaller wavelengths are slightly further amplified for the lowest

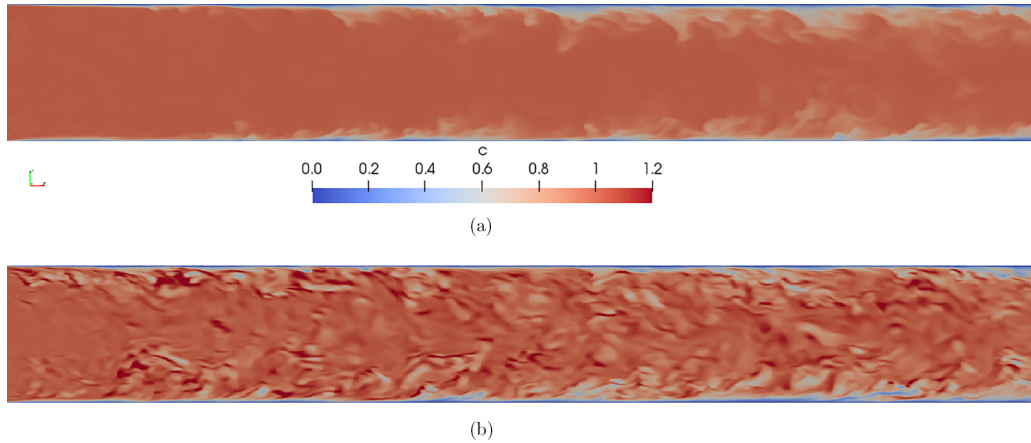


FIG. 7. Instantaneous contours of particle concentration at  $Re = 10300$  for (a)  $St^+ = 0.0$  and (b)  $St^+ = 1$  with  $1/Fr_z = 0$  (no gravity case).

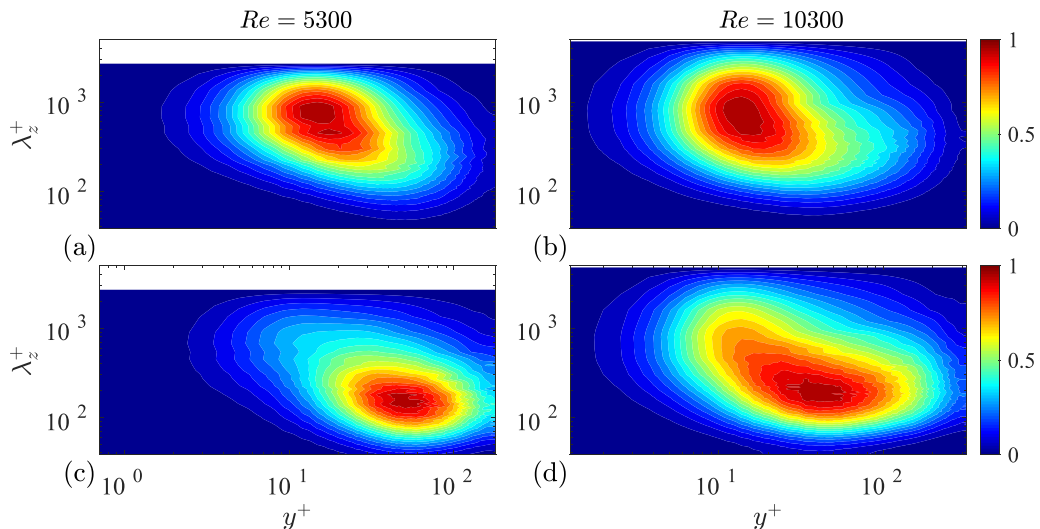


FIG. 8. Premultiplied spectra of particle concentration in the streamwise direction (averaged over the azimuthal direction) for (a), (c)  $Re = 5300$  and (b), (d)  $Re = 10300$ . In panels (a) and (b)  $St^+ = 0$  and in panels (c) and (d)  $St^+ = 1.0$ . Gravity is omitted,  $1/Fr_z = 0$ . The plots are normalized so the maximum energy is unity.

Re number. However, for the larger Re there are essentially no differences between upward and downward flow.

In Fig. 8, the premultiplied streamwise spectra  $k_z E_{c_h, c_h}$  averaged over the  $\theta$  direction are plotted at different wall-normal distances  $y^+$  for  $St^+ = 0$  (top row) and  $St^+ = 1$  (bottom row) and Reynolds numbers  $Re = 5300$  and  $10300$ , with gravity omitted  $1/Fr_z = 0$ . Close to the wall, the spectra for  $St^+ = 0$  in Figs. 8(a) and 8(b) are qualitatively similar to the spectra of the streamwise fluctuating velocity field (omitted here for brevity). The peak is located at  $(y^+, \lambda_z^+) \approx (15, 1000)$ , thus the scalar streaks have very similar characteristic dimensions as the velocity streaks. Further away from the wall, energy is concentrated at smaller wavelengths; these findings are in accordance with Refs. [62,63]. For  $St^+ = 1$  however, the picture is different. While close to the wall the spectra are similar to passive scalar and the length scales decrease away from the wall, the spectral peak has moved from the buffer layer to the logarithmic region, and it is now located at  $(y^+, \lambda_z^+) \approx (50, 150)$ . Further away from the wall, the dominant streamwise length scale remains almost constant. This once again agrees with the contour plots of Fig. 7. Increasing the Reynolds number results in a qualitatively similar picture; the peak is shifted to lower wavelengths and into the logarithmic region of the flow. For the  $Re = 10300$  case there is a relatively larger amount of energy in the high wavelength region close to the wall.

The shift of the peak to smaller length scales is due to inertial clustering, as explained earlier. The displacement to the logarithmic layer is more difficult to explain. It is very likely caused by the imposed boundary conditions. The values of both velocity and particle concentration are zero at the wall, and for small  $y^+$  values (less than 10) the spectra are similar. Further away from the wall the effect of the boundary condition is weakened and inertial clustering takes over.

In Fig. 9, the streamwise spectra are plotted for Froude numbers  $Fr_z = \pm 0.4$  for  $St^+ = 1$  and  $Re = 5300$  and  $10300$ . The same overall trends are observed as for the no-gravity case of Fig. 8. The main difference is in the bulk of the flow, where it seems the downward flow (top row) has structures with slightly larger wavelengths compared with the upward flow (bottom row); this can be seen by comparing the top-right corners of the two panels, and is more evident for the low Re number case (left column). From this figure it is clear that the effect of Re is stronger than the

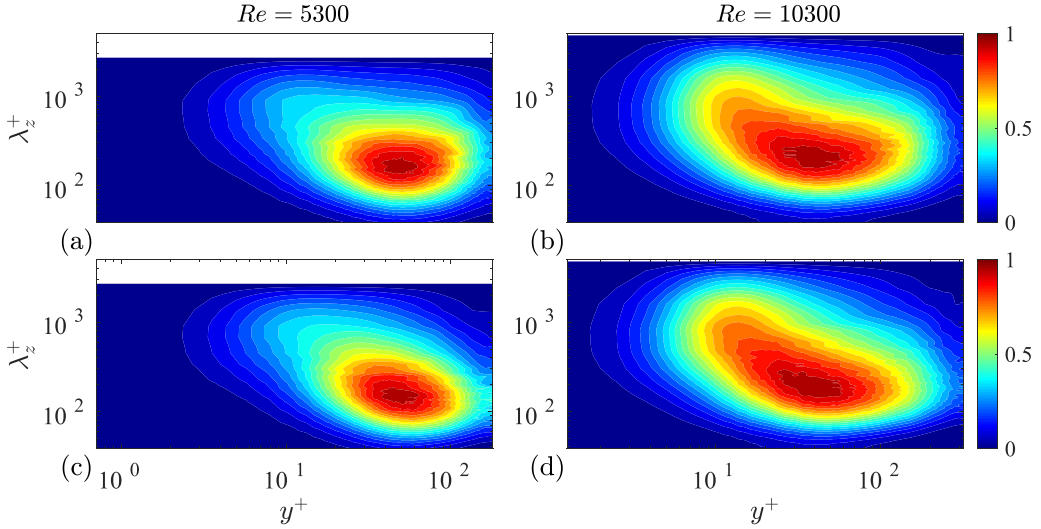


FIG. 9. Premultiplied spectra of particle concentration fluctuations in the streamwise direction (averaged over the azimuthal direction) for (a), (c)  $Re = 5300$  and (b), (d)  $Re = 10300$ . In panels (a) and (b)  $Fr_z = 0.4$  and in panels (c) and (d)  $Fr_z = -0.4$ . In all plots  $St^+ = 1$ . The plots are normalized so the maximum energy is unity.

effect of gravity. In Fig. 10, the premultiplied spectra in the azimuthal direction  $k_\theta E_{c_\theta c_\theta}$  are plotted in the  $(y^+, \lambda_\theta^+)$  plane, for  $St^+ = 0$  and 1,  $Re = 5300$  and 10300, and  $1/Fr_z = 0$  (effect of gravity omitted). The spectral peak is located at  $\lambda_\theta^+ = 100$  regardless of Stokes and Reynolds numbers. For  $Re = 5300$  and  $St^+ = 1$  the peak moves in the logarithmic region, consistent with the results of Fig. 8. For  $Re = 10300$  the shift of the peak is very small, but the energy is significantly increased in

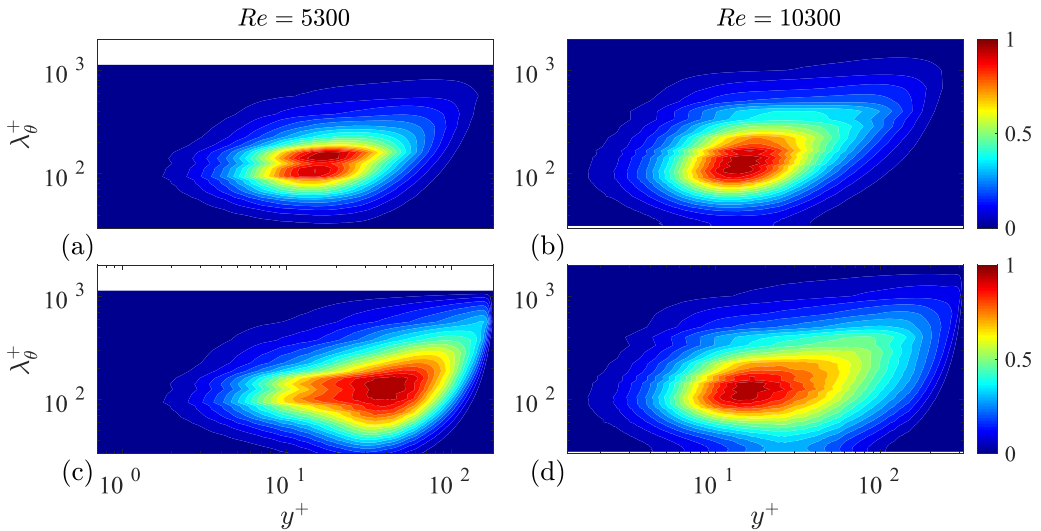


FIG. 10. Premultiplied spectra of particle concentration fluctuations in the azimuthal direction (averaged over the streamwise direction) for (a), (c)  $Re = 5300$  and (b), (d)  $Re = 10300$ . In panels (a) and (b)  $St^+ = 0$  and in panels (c) and (d)  $St^+ = 1.0$ . Gravity is omitted,  $1/Fr_z = 0$ . The plots are normalized so the maximum energy is unity.

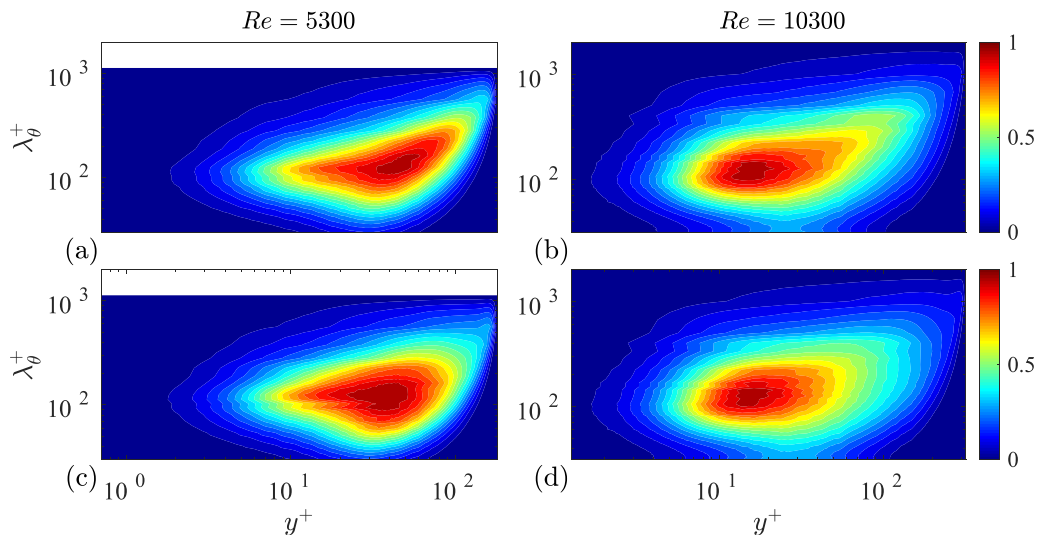


FIG. 11. Premultiplied spectra of particle concentration fluctuations in the azimuthal direction (averaged over the streamwise direction) for (a), (c)  $Re = 5300$  and (b), (d)  $Re = 10300$ . In panels (a) and (b)  $Fr_z = 0.4$  and in panels (c) and (d)  $Fr_z = -0.4$ . In all plots  $St^+ = 1$ . The plots are normalized so the maximum energy is unity.

the logarithmic region (compare top and bottom panels of Fig. 10 in the right column); this indicates that the peak becomes broader and less sharp. As observed in Figs. 6 and 8, the effect of the Stokes number is larger for the lower Reynolds number so it is likely that the peak would shift towards the log-layer for larger Stokes number.

Finally, in Fig. 11, the effect of gravity of the premultiplied spectra in the  $(y^+, \lambda_\theta^+)$  plane is examined for Froude numbers  $Fr_z = \pm 0.4$  and Reynolds numbers  $Re = 5300$  and  $10300$ ; the Stokes number is kept constant at  $St^+ = 1$ . As in Fig. 10, the peak location of the azimuthal wavelength does not change significantly. The downward flow seems to somewhat increase the energy of the large wavelengths near the center, and for the upward flow the peak is slightly closer to the wall.

## B. POD modes

The normalized particle concentration field  $c_h$  is Fourier transformed into the azimuthal and streamwise directions and for each wave number pair  $(k_z, k_\theta)$  POD modes are extracted, as explained in Sec. II C. We denote with  $n$  the mode order for each pair.

We compute the ratio  $\lambda_1/\lambda_T$  (where  $\lambda_1$  is the dominant, i.e.  $n = 1$ , eigenvalue for each pair, and  $\lambda_T$  is the concentration variance integrated over the pipe volume) and sum over all  $k_z$  wave numbers. The result denotes the fraction of the variance contained in the dominant POD mode across all streamwise wave numbers and is plotted against  $k_\theta$  in Fig. 12. The peak for  $Re = 5300$  is at  $k_\theta = 3$ , while for  $Re = 10300$  is at  $k_\theta = 4$ , regardless of Stokes or Froude numbers. The fraction of the variance contained in the dominant mode is reduced for  $St^+ = 1$  compared with  $St^+ = 0$ . This means that higher-order modes become more prevalent. It is well known, see Duggleby *et al.* [64], that higher-order modes are oscillatory in the radial direction, thus represent smaller scales. Increasing the Stokes number results in smaller scales, as seen in Fig. 7, and this explains why modes with  $n > 1$  assume a larger role. Gravity seems to have a secondary effect on the eigenvalue distribution, especially for the lower  $Re$ . Upward flow ( $Fr_z < 0$ ) amplifies small wave numbers, while downward flow ( $Fr_z > 0$ ) suppresses small wave numbers.

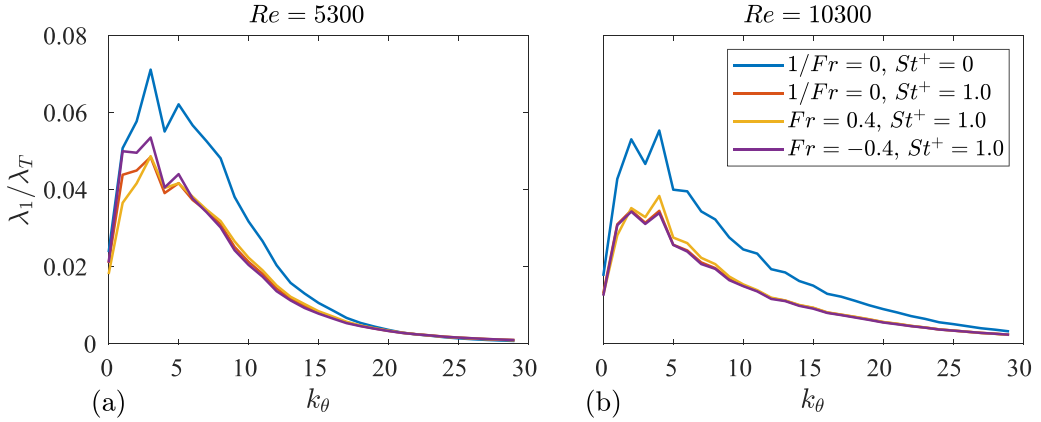


FIG. 12. Eigenvalue distribution of the dominant particle concentration POD mode over  $k_\theta$  for (a)  $Re = 5300$  and (b)  $Re = 10300$ .

The ratio  $\lambda_1/\lambda_T$  is also summed over all azimuthal wave numbers and plotted against  $k_z$  in Fig. 13. The peak in all cases is at  $k_z = 1$  (in agreement with Ref. [64] for the velocity field), but it is reduced significantly for  $St^+ = 1$  compared with  $St^+ = 0$  in all cases, again in agreement with Fig. 7.

In Fig. 14, the ratios  $\lambda_n/\lambda_T$  are summed across all wave numbers in both azimuthal and streamwise directions and plotted against  $n$ . For the low-inertia particles the variance fraction of the dominant mode is smaller compared with passive scalar, and larger for the higher-order modes. This is consistent with the previous figures. Gravity plays no role for both  $Re$  numbers.

In Fig. 15 we analyze the shapes of the dominant ( $n = 1$ ) POD modes. We have limited the analysis to wave numbers  $k_\theta = 4, 7$  and  $k_z = 1$ . The modes have similar shapes. The peaks are closer to the wall for the higher Reynolds number as expected (the horizontal axis is in physical units). Although gravity does not affect much the energy content as shown in the previous figures, it has a more noticeable effect on the mode shapes, especially for downward flow. In this case, the modes with  $k_\theta = 4$  (top row) have more pronounced presence in the bulk of the flow; notice also

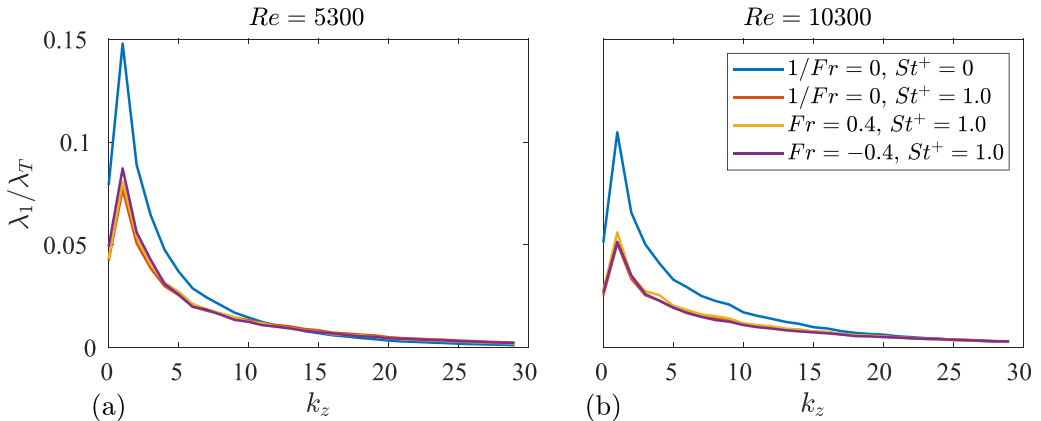


FIG. 13. Eigenvalue distribution of the dominant particle concentration POD mode over  $k_z$  for (a)  $Re = 5300$  and (b)  $Re = 10300$ .

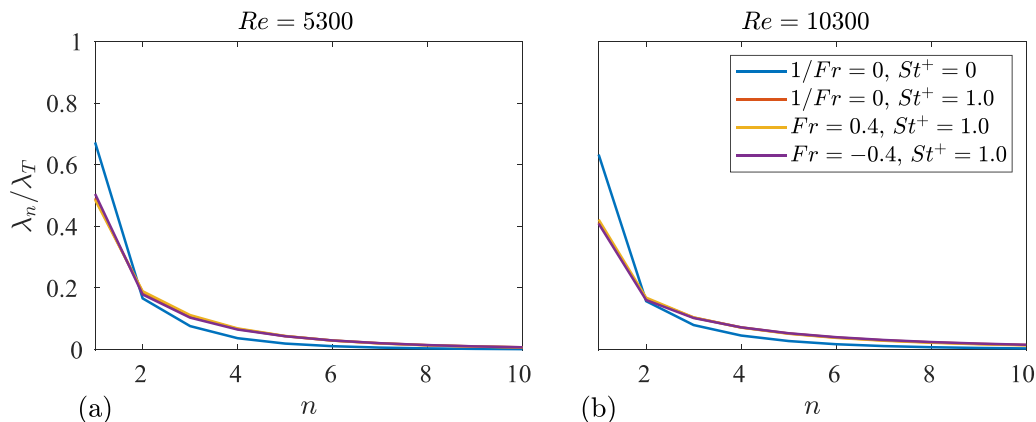


FIG. 14. Eigenvalue distribution of the particle concentration POD modes,  $n$ , normalized with the total particle concentration variance, integrated over streamwise mode numbers  $k_z$  and azimuthal wave numbers  $k_\theta$ , for (a)  $Re = 5300$  and (b)  $Re = 10300$ .

that a second peak appears closer to the center for both  $Re$  numbers. For modes with  $k_\theta = 7$  (bottom row) that have less energy (see Fig. 12) the effect of gravity is less noticeable.

Contour plots of the modes with  $k_\theta = 4$  in streamwise and cross-stream planes are shown in Fig. 16. There are small differences between  $St^+ = 0$  and 1 in the no-gravity case (top row), but the two peaks in the radial direction for the downward flow can be clearly noticed in the bottom-left figure (red region peaks closer to the wall and blue region further away from the wall).

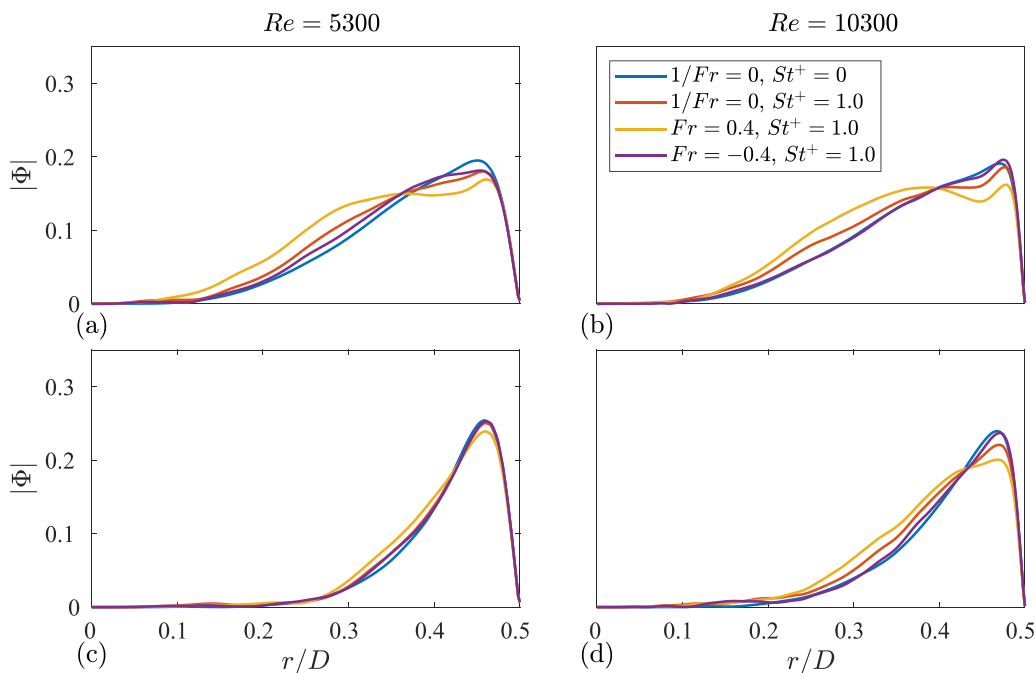


FIG. 15. Particle concentration POD modes for (a), (b)  $k_z = 1$ ,  $k_\theta = 4$ ,  $n = 1$  and (c), (d)  $k_z = 1$ ,  $k_\theta = 7$ ,  $n = 1$  at (a), (c)  $Re = 5300$  and (b), (d)  $Re = 10300$ .

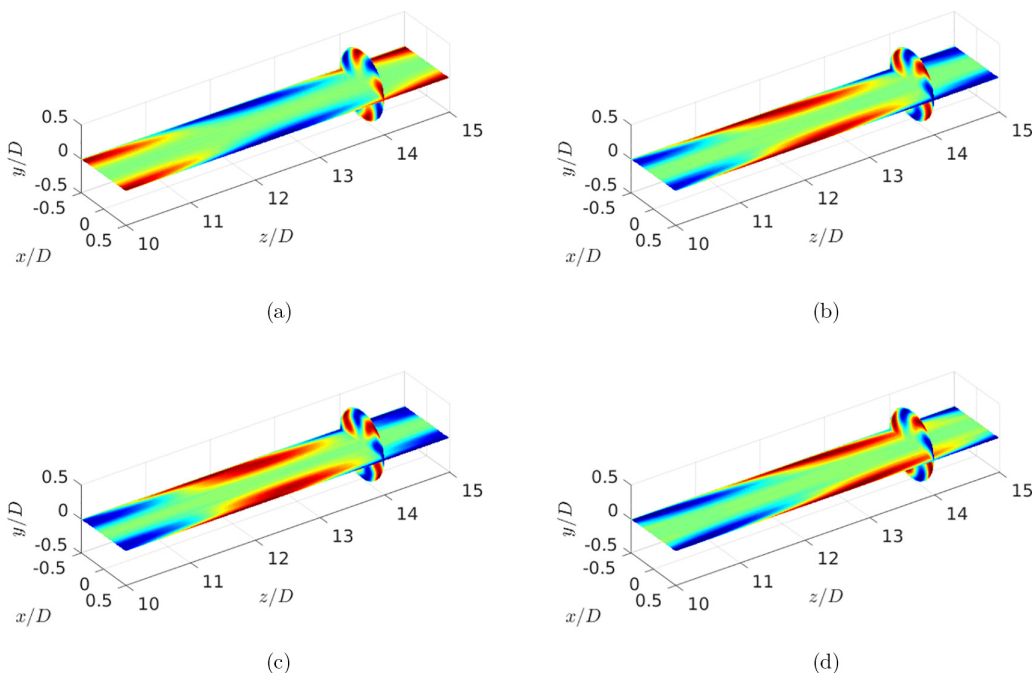


FIG. 16. Dual-plane contour plots of the particle concentration POD modes at (a)  $Re = 5300$  for  $k_z = 1$ ,  $k_\theta = 4$ ,  $n = 1$  and  $St^+ = 0$ ,  $1/Fr = 0$ , (b)  $St^+ = 1$ ,  $1/Fr = 0$ , (c)  $St^+ = 1$ ,  $Fr_z = 0.4$ , and (d)  $St^+ = 1$ ,  $Fr_z = -0.4$ .

### C. EPOD modes and analysis of deposition with the aid of the FIK identity

As shown in Sec. III, inertia adds three new terms to the FIK identity, but for  $z > 10D$  only  $Sh_{\text{FIK},\text{Ir}}$  contributes to deposition, refer to Fig. 3. Thus the contribution of turbulent fluctuations to  $Sh$  can be written as

$$Sh_{\text{turb}} = Sh_{\text{FIK},2} + Sh_{\text{FIK},\text{Ir}}. \quad (26)$$

Substituting decomposition (18) of the fluctuating particle concentration field and (correlated) velocity field into the analytic expressions of  $Sh_{\text{FIK},2}$  and  $Sh_{\text{FIK},\text{Ir}}$  [see equations (21) and (22), respectively], we can calculate the contribution of each POD and EPOD mode pair to the time-average deposition.

We start by evaluating the contribution to  $Sh_{\text{turb}}$  of the first (dominant,  $n = 1$ ) POD or EPOD mode summed over all streamwise wave numbers and plot the result against  $k_\theta$  in Fig. 17. The peak is located at  $k_\theta = 3$  or 4 for the low and high Reynolds numbers, respectively. When gravity is omitted, Stokes number does not seem to have an effect, although the eigenvalue of the first mode pair is smaller for  $St^+ = 1$ , as shown in Fig. 14. The effect of gravity is more pronounced for downward flow where the contribution of the dominant POD mode is weaker. This is probably because of the shape of the modes that become more uniform, have a suppressed peak close to the wall (see Figs. 15 and 16) and thus less effective at wall deposition due to the  $r^2$  weighting in  $Sh_{\text{FIK},2}$ , see equation (21).

The contribution of the dominant modes to the particle inertia term  $Sh_{\text{FIK},\text{Ir}}$  (summed over all  $k_z$ ) is depicted in Fig. 18. The effect of gravity can be more clearly seen in this plot. For both  $Re$  numbers, inertia effects are strongest for downward flow and weakest for upward flow. Modes with low azimuthal wave numbers,  $k_\theta = 1-3$ , contribute most to deposition; instead the highest concentration variance is contained in modes  $k_\theta = 3-7$ , refer to Fig. 17.

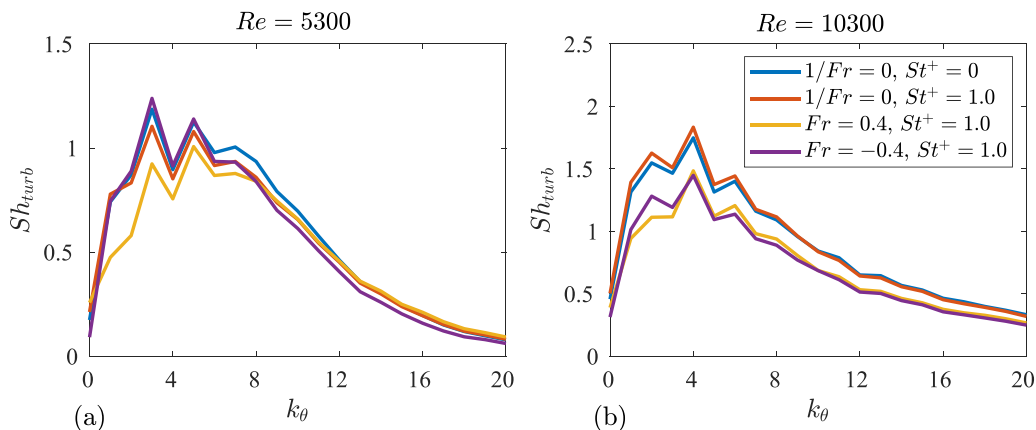


FIG. 17. Contribution to  $Sh_{\text{turb}}$  of the dominant mode ( $n = 1$ ) summed over all streamwise wave numbers for (a)  $Re = 5300$  and (b)  $Re = 10300$ .

Attention is now turned to the number of POD modes that are required to reconstruct  $Sh_{\text{turb}}$ . To this end, we evaluate the cumulative  $Sh_{\text{turb}}$  for  $k_{\theta} = 1-30$  and for  $n = 1$  and  $n = 1-50$  for different  $k_z$  values. The results are plotted in Fig. 19 for  $Re = 5300$ . For all cases, with  $k_{\theta} = 1-15$ ,  $k_z = 1-10$ , and  $n = 1$ , it is possible to reconstruct roughly 70% of the total deposition arising from turbulent fluctuations; the value changes slightly with Stokes and Froude numbers. This corresponds to 150 modes out of the total number of  $64 \times 128 \times 600 \approx 5 \times 10^6$  (i.e., only 0.003% of the modes are required). Inertia seems to increase the contribution from the largest wave numbers, especially for  $n = 1-50$ .  $Sh_{\text{turb}}$  is found to be 20% higher for  $St^+ = 1$  when calculated for  $k_z = 11-20$ . This is consistent with the observation that the Stokes number results in smaller structures in the flow. The upward flow seems to require fewer POD modes compared with the downward flow. This is visible in the  $k_z = 1-5$  line in Fig. 19, where the  $n = 1-50$  dashed line almost overlaps with the  $n = 1$  solid line in the case of the upward flow, but the two lines are further apart in the case of the downward flow. For  $Re = 10300$  (plot not shown for brevity), a larger number of modes are required for the reconstruction. Using 150 modes will now only reconstruct 40%–50% of  $Sh_{\text{turb}}$ . The observations regarding the effect of Stokes number and gravity remain the same.

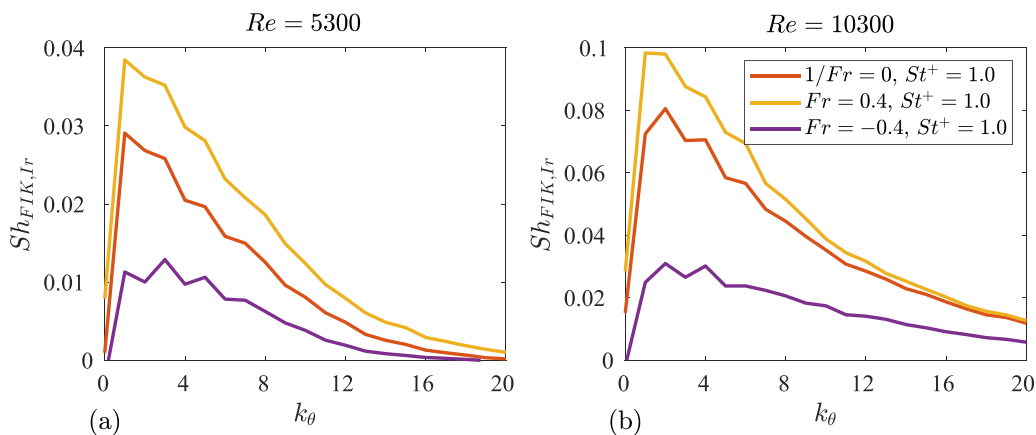


FIG. 18. Contribution to  $Sh_{\text{FIK,Ir}}$  of the dominant mode ( $n = 1$ ) summed over all streamwise wave numbers for (a)  $Re = 5300$  and (b)  $Re = 10300$ .

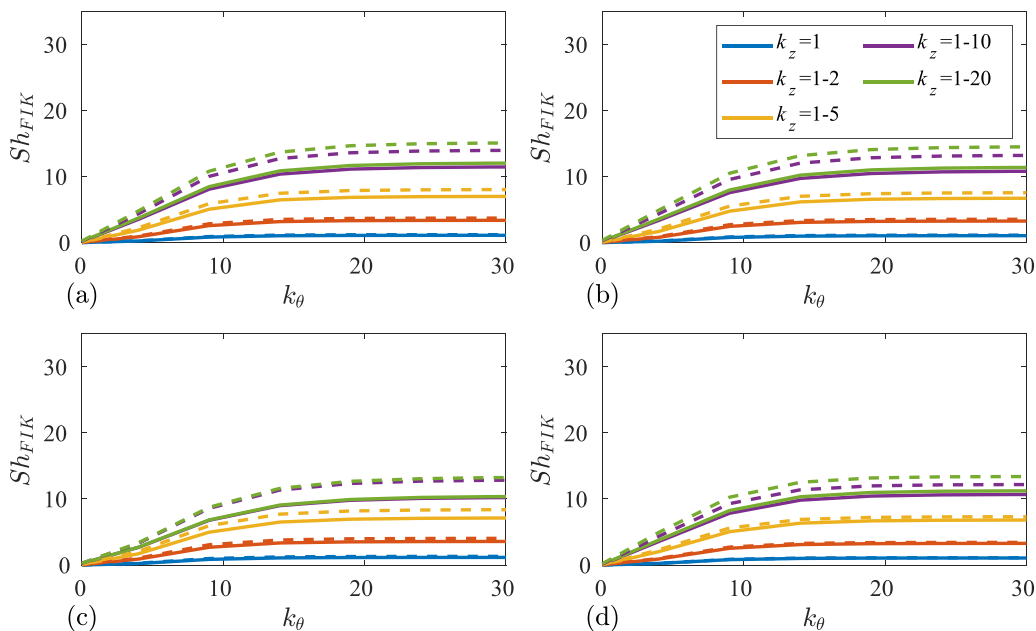


FIG. 19. Cumulative plot of  $Sh_{\text{turb}}$  against  $k_\theta$  for different  $k_z$  values at  $Re = 5300$ . The solid lines denote  $n = 1$ , and the dashed lines  $n = 1-50$ , where panel (a) is for  $St^+ = 0$ ,  $1/Fr_z = 0$ , panel (b) is for  $St^+ = 1$ ,  $1/Fr_z = 0$ , panel (c) is for  $St^+ = 1$ ,  $Fr_z = 0.4$ , and panel (d) is for  $St^+ = 1$ ,  $Fr_z = -0.4$ .

## V. CONCLUSIONS

We investigate the role of coherent structures on the transport and wall deposition of low-inertia particles in a turbulent pipe flow at  $Re = 5300$  and  $Re = 10\,300$  (based on bulk velocity). We employ the equilibrium Eulerian approach to model particle velocity and concentration. The model is valid only for particles with low Stokes number but captures important physical aspects, such as inertial clustering and turbophoresis. This approach has allowed us to study particle transport and deposition with the same techniques that are employed for passive scalar transport, namely, POD and extended POD. To the best of our knowledge, this is the first time these two techniques are applied to analyze particle transport.

We aim to analyze individual coherent structures and their contribution to the time-average rate of particle deposition at the wall. Toward this end, we derive a new FIK identity that provides explicit analytical expressions for the contributions of inertia terms to deposition. We then examine the spectra of particle concentration fluctuations and compare them with the spectra of passive scalar to reveal the roles of inertia and gravity.

The premultiplied spectra of the particle concentration field clearly demonstrate that smaller wavelengths are amplified when the Stokes number is increased. The peak of the streamwise spectra in the wall-normal direction shifts from  $\lambda_z^+ \approx 1000$  to  $\approx 150$  and from the buffer layer,  $y^+ \approx 15$  to the logarithmic layer  $y^+ \approx 50$  of the pipe. The main effect of gravity seems to amplify larger wavelengths further from the wall for a downward flow and reduce the same structures for the upward flow. This can be observed for both Reynolds numbers but it is more pronounced for  $Re = 5300$ .

The particle concentration modes were identified with POD, while the flow structures correlated with the particle concentration structures were extracted using Extended POD. Both velocity and normalized particle concentration fields were first Fourier transformed in the homogeneous azimuthal and streamwise directions. Increasing Stokes number reduces the fraction of the variance

contained in the first POD mode and increases the fraction of higher other modes. Visualization of the modes allows us to gain insight into how inertia and gravity affect particle transport behavior.

Using the FIK identity, we evaluated the contribution of turbulent particle flux to the time-average deposition rate or Sherwood number  $Sh$ . Approximately 70% of  $Sh$  is due to velocity and concentration correlations; the exact value depends on the Reynolds, Stokes, and Froude numbers. POD and EPOD modes were subsequently employed to decompose the correlations and analyze the contribution of individual modes to  $Sh$ . In the  $Re = 5300$  flow, mode  $k_\theta = 3$  contributes the most to the deposition, and in  $Re = 10\,300$  it is mode  $k_\theta = 4$ . About 70% of the deposition can be reconstructed using 150 POD modes in the  $Re = 5300$  flow and 40%–50% in the  $Re = 10\,300$ , depending on Stokes number and direction of gravity.

The methodology developed can be applied to higher Reynolds numbers to quantify the effect of large- and very-large-scale flow structures on particle deposition to the wall. In this case, care should be exercised to make sure that the range of validity of the Eulerian equilibrium model is satisfied. As  $Re$  increases, the Kolmogorov timescale  $\tau_k$  decreases, so only particles with correspondingly smaller relaxation time  $\tau$  can be considered. It is well known that large structures leave their footprint at the wall but their contribution to deposition is not well understood. This knowledge can be exploited for active or passive control of deposition, in the same way that the understanding of the effect of different flow structures in the skin friction has recently led to the development of drag-reducing actuation strategies that offer net power savings even for large  $Re$  numbers, see Ref. [65]. Finally, the methodology can be also employed to provide insight into more complex flow settings that may include two-way coupling, chemical reactions, and different geometries.

#### ACKNOWLEDGMENTS

The authors would like to thank the UK Turbulence Consortium [67] for providing computational time on ARCHER2 via EPSRC Grant No. EP/R029326/1. We are also grateful to the UK Materials and Molecular Modelling Hub (EP/P020194/1) for computational resources on YOUNG. The authors would also like to acknowledge the financial support from the Leverhulme Trust (Grant No. RPG-2018-101). George Papadakis is supported by EPSRC Grants No. EP/X017273/1, No. EP/W001748/1, and No. EP/W00481X/1.

#### APPENDIX: DERIVATION OF FIK IDENTITY FOR DEPOSITION OF LOW-INERTIA PARTICLES

The particle velocity field is obtained from the Eulerian equilibrium model of Ferry *et al.* [21], see equation (5), and can be written in dimensionless form in polar coordinates as

$$v_r = u_r - \text{St} \left( \frac{\partial u_r}{\partial t} + \frac{1}{r} \frac{\partial r u_r^2}{\partial r} + \frac{1}{r} \frac{\partial u_r u_\theta}{\partial u_\theta} + \frac{\partial u_z u_r}{\partial z} - \frac{u_\theta^2}{r} \right), \quad (\text{A1})$$

$$v_z = u_z + \frac{\text{St}}{\text{Fr}_z} - \text{St} \left( \frac{\partial u_z}{\partial t} + \frac{1}{r} \frac{\partial r u_r u_z}{\partial r} + \frac{1}{r} \frac{\partial u_\theta u_z}{\partial \theta} + \frac{\partial u_z^2}{\partial z} \right). \quad (\text{A2})$$

The derivation of the FIK identity follows the process of Kasagi *et al.* [66] and Schlander *et al.* [38]. In the transport equation (6), distances are normalized with radius  $R$ , velocities with twice the bulk velocity,  $2U_B$  and the particle concentration with the inlet concentration,  $c_I$ . Reynolds averaging (6), taking into account that  $\bar{u}_r = 0$ , and that the particulate flow is homogeneous in the azimuthal direction, i.e.,  $\bar{v}_\theta = 0$ ,  $\partial \bar{c} / \partial \theta = 0$ , we get

$$\frac{\partial \overline{u_r' c'}}{\partial r} + \bar{I}_{z, \text{passive}} + \text{St} \frac{\partial \bar{I}_r}{\partial r} + \text{St} \bar{I}_z + \frac{\text{St}}{\text{Fr}} \frac{\partial \bar{c}}{\partial z} = \frac{1}{\text{ReSc}} \left[ \frac{1}{r} \frac{\partial}{\partial r} \left( r \frac{\partial \bar{c}}{\partial r} \right) \right], \quad (\text{A3})$$

where

$$\bar{I}_{z,\text{passive}} = -\frac{1}{\text{Re Sc}} \frac{\partial^2 \bar{c}}{\partial z^2} + \frac{\partial \bar{u}_z \bar{c}}{\partial z} + \frac{\partial \bar{u}_z' c'}{\partial z}, \quad (\text{A4})$$

$$\bar{I}_r = -\left( \frac{\partial \bar{u}_r' u_r' \bar{c}}{\partial r} + \frac{\bar{u}_r'^2 - \bar{u}_\theta'^2}{r} \bar{c} + \frac{\bar{u}_r'^2 c' - \bar{u}_\theta'^2 c'}{r} + \frac{\partial \bar{u}_r' u_r' c'}{\partial r} + \frac{\partial \bar{u}_r' u_z' c'}{\partial z} + \bar{u}_z \frac{\partial \bar{u}_r' c'}{\partial z} \right), \quad (\text{A5})$$

$$\bar{I}_z = -\frac{\partial}{\partial z} \left( \frac{\bar{u}_r' u_z' \bar{c} + \bar{u}_r' u_z' c' + \bar{u}_z \bar{u}_r' c'}{r} + \bar{u}_z \frac{\partial \bar{u}_r' c'}{\partial r} + \frac{\partial \bar{u}_r' u_z' \bar{c}}{\partial r} + \frac{\partial \bar{u}_r' u_z' c'}{\partial r} + 2\bar{u}_z \frac{\partial \bar{u}_z' c'}{\partial z} + \frac{\partial \bar{u}_z'^2 c'}{\partial z} \right). \quad (\text{A6})$$

$\bar{I}_{z,\text{passive}}$  is the streamwise inhomogeneity term,  $\bar{I}_r$  and  $\bar{I}_z$  are new terms that arise because the particle velocity is different from the fluid velocity.

The Sherwood number is defined as

$$\text{Sh} = \frac{2kR}{\Gamma_C} = -2 \left. \frac{d\bar{c}}{dr} \right|_{\text{wall}} \frac{1}{\bar{c}_B - \bar{c}_W}, \quad (\text{A7})$$

where  $k = J_w / (\bar{c}_B - \bar{c}_W)$  is the deposition rate coefficient,  $J_w = \Gamma_C \partial \bar{c} / \partial r$  is the wall flux, and  $\Gamma_C$  is the diffusivity.

Equation (A3) is integrated over the cross section of the pipe to give

$$\begin{aligned} 0 &= \int_0^1 \frac{1}{r} \frac{\partial}{\partial r} r \left[ \bar{u}_r' c' + \text{St} \bar{I}_r - \frac{1}{\text{Re Sc}} \frac{\partial \bar{c}}{\partial r} \right] r dr + \int_0^1 \left( \bar{I}_{z,\text{passive}} + \text{St} \bar{I}_z + \frac{\text{St}}{\text{Fr}} \frac{\partial \bar{c}}{\partial z} \right) r dr, \\ \implies 0 &= -\left. \frac{1}{\text{Re Sc}} \frac{d\bar{c}}{dr} \right|_{\text{wall}} + \int_0^1 \left( \bar{I}_{z,\text{passive}} + \text{St} \bar{I}_z + \frac{\text{St}}{\text{Fr}} \frac{\partial \bar{c}}{\partial z} \right) r dr. \end{aligned} \quad (\text{A8})$$

The above equation is now multiplied by two and subtracted from (A3):

$$0 = \frac{1}{r} \frac{\partial}{\partial r} r \left[ \bar{u}_r' c' + \text{St} \bar{I}_r - \frac{1}{\text{Re Sc}} \frac{\partial \bar{c}}{\partial r} \right] + \langle \bar{I}_{z,\text{passive}} \rangle + \text{St} \langle \bar{I}_z \rangle + \frac{\text{St}}{\text{Fr}} \left\langle \frac{\partial \bar{c}}{\partial z} \right\rangle + \left. \frac{2}{\text{Re Sc}} \frac{d\bar{c}}{dr} \right|_{\text{wall}}, \quad (\text{A9})$$

where the angular brackets  $\langle \cdot \rangle$  define the operator  $\langle f \rangle = f - 2 \int_0^1 f r dr$  for the general variable  $f$ . Integrating equation (A9) over a cross section of radius  $r$  we get

$$\begin{aligned} 0 &= \int_0^r \frac{1}{r} \frac{\partial}{\partial r} r \left[ \bar{u}_r' c' + \text{St} \bar{I}_r - \frac{1}{\text{Re Sc}} \frac{\partial \bar{c}}{\partial r} \right] r dr \\ &+ \int_0^r \left( \langle \bar{I}_{z,\text{passive}} \rangle + \text{St} \langle \bar{I}_z \rangle + \frac{\text{St}}{\text{Fr}} \left\langle \frac{\partial \bar{c}}{\partial z} \right\rangle \right) r dr + \int_0^r \left. \frac{2}{\text{Re Sc}} \frac{d\bar{c}}{dr} \right|_{\text{wall}} r dr, \\ \implies \frac{\text{Sh}(\bar{c}_B - \bar{c}_W)}{\text{Re Sc}} \frac{r^2}{2} &= r \left[ \bar{u}_r' c' + \text{St} \bar{I}_r - \frac{1}{\text{Re Sc}} \frac{\partial \bar{c}}{\partial r} \right] + \int_0^r \left( \langle \bar{I}_{z,\text{passive}} \rangle + \text{St} \langle \bar{I}_z \rangle + \frac{\text{St}}{\text{Fr}} \left\langle \frac{\partial \bar{c}}{\partial z} \right\rangle \right) r dr, \end{aligned} \quad (\text{A10})$$

where the definition of Sherwood number, equation (A7), was used. Finally, (A10) is integrated again over the cross section of the pipe,

$$\begin{aligned} &\int_0^1 \frac{\text{Sh}(\bar{c}_B - \bar{c}_W)}{\text{Re Sc}} \frac{r^2}{2} r dr \\ &= \int_0^1 r \left[ \bar{u}_r' c' + \text{St} \bar{I}_r - \frac{1}{\text{Re Sc}} \frac{\partial \bar{c}}{\partial r} \right] r dr + \int_0^1 \left[ \int_0^r \left( \langle \bar{I}_{z,\text{passive}} \rangle + \text{St} \langle \bar{I}_z \rangle + \frac{\text{St}}{\text{Fr}} \left\langle \frac{\partial \bar{c}}{\partial z} \right\rangle \right) r dr \right] r dr, \\ &\implies \frac{\text{Sh}(\bar{c}_B - \bar{c}_W)}{\text{Re Sc}} \frac{1}{8} \end{aligned}$$

$$\begin{aligned}
 &= \int_0^1 r(\overline{u'_r c'} + \text{St}\bar{I}_r) r dr - \frac{1}{\text{Re Sc}} \int_0^1 r \frac{\partial \bar{c}}{\partial r} r dr \\
 &\quad + \int_0^1 \left[ \int_0^r \left( \langle \bar{I}_{z, \text{passive}} \rangle + \text{St} \langle \bar{I}_z \rangle + \frac{\text{St}}{\text{Fr}} \left\langle \frac{\partial \bar{c}}{\partial z} \right\rangle \right) r dr \right] r dr.
 \end{aligned} \tag{A11}$$

Using integration by parts, the final expression for Sh becomes,

$$\begin{aligned}
 \text{Sh} &= -\frac{8}{(\bar{c}_B - \bar{c}_W)} \int_0^1 r \frac{\partial \bar{c}}{\partial r} r dr + \frac{8\text{ReSc}}{(\bar{c}_B - \bar{c}_W)} \int_0^1 r(\overline{u'_r c'} + \text{St}\bar{I}_r) r dr \\
 &\quad + \frac{4\text{ReSc}}{(\bar{c}_B - \bar{c}_W)} \int_0^1 (1-r^2) \left( \left\langle \frac{\partial \bar{u}_z \bar{c}}{\partial z} \right\rangle + \left\langle \frac{\partial \overline{u'_z c'}}{\partial z} \right\rangle + \text{St} \langle \bar{I}_z \rangle + \frac{\text{St}}{\text{Fr}} \left\langle \frac{\partial \bar{c}}{\partial z} \right\rangle \right) r dr \\
 &\quad - \frac{4}{(\bar{c}_B - \bar{c}_W)} \int_0^1 (1-r^2) \left\langle \frac{\partial^2 \bar{c}}{\partial z^2} \right\rangle r dr,
 \end{aligned} \tag{A12}$$

where

$$\bar{I}_r = -\left( \frac{\partial \overline{u'_r u'_r} \bar{c}}{\partial r} + \frac{\overline{u_r^2} - \overline{u_\theta^2}}{r} \bar{c} + \frac{\overline{u'_r c'} - \overline{u_\theta^2 c'}}{r} + \frac{\partial \overline{u'_r u'_r}}{\partial r} \bar{c}' + \frac{\partial \overline{u'_r u'_z}}{\partial z} \bar{c}' + \overline{u_z} \frac{\partial \overline{u'_r c'}}{\partial z} \right), \tag{A13}$$

and

$$\bar{I}_z = -\frac{\partial}{\partial z} \left( \frac{\overline{u'_r u'_z} \bar{c} + \overline{u'_r u'_z c'} + \overline{u_z u'_r c'}}{r} + \overline{u_z} \frac{\partial \overline{u'_r}}{\partial r} \bar{c}' + \frac{\partial \overline{u'_r u'_z}}{\partial r} \bar{c} + \frac{\partial \overline{u'_r u'_z}}{\partial r} \bar{c}' + 2\overline{u_z} \frac{\partial \overline{u'_z}}{\partial z} \bar{c}' + \frac{\partial \overline{u_z^2}}{\partial z} \bar{c}' \right). \tag{A14}$$

Form (A12) is used in the rest of the paper.

- 
- [1] A. J. Smits, B. J. McKeon, and I. Marusic, High-Reynolds number wall turbulence, *Annu. Rev. Fluid Mech.* **43**, 353 (2011).
  - [2] S. J. Kline, W. C. Reynolds, F. A. Schraub, and P. W. Runstadler, The structure of turbulent boundary layers, *J. Fluid Mech.* **30**, 741 (1967).
  - [3] T. Theodorsen, Mechanism of turbulence, *Proc. 2nd Midwestern Conference on Fluid Mech* (1952), pp. 1–19.
  - [4] N. Hutchins and I. Marusic, Evidence of very long meandering features in the logarithmic region of turbulent boundary layers, *J. Fluid Mech.* **579**, 1 (2007).
  - [5] B. J. McKeon, The engine behind (wall) turbulence: Perspectives on scale interactions, *J. Fluid Mech.* **817**, 1 (2017).
  - [6] J. Jiménez, Coherent structures in wall-bounded turbulence, *J. Fluid Mech.* **842**, P1 (2018).
  - [7] K. D. Squires and J. K. Eaton, Measurements of particle dispersion obtained from direct numerical simulations of isotropic turbulence, *J. Fluid Mech.* **226**, 1 (1991).
  - [8] M. Caporaloni, F. Tampieri, F. Trombetti, and O. Vittori, Transfer of particles in nonisotropic air turbulence, *J. Atmos. Sci.* **32**, 565 (1975).
  - [9] M. W. Reeks, The transport of discrete particles in inhomogeneous turbulence, *J. Aerosol Sci.* **14**, 729 (1983).
  - [10] D. W. Rouson and J. K. Eaton, On the preferential concentration of solid particles in turbulent channel flow, *J. Fluid Mech.* **428**, 149 (2001).
  - [11] C. Narayanan, D. Lakehal, L. Botto, and A. Soldati, Mechanisms of particle deposition in a fully developed turbulent open channel flow, *Phys. Fluids* **15**, 763 (2003).

- [12] W. S. Uijttewaala and R. V. Oliemans, Particle dispersion and deposition in direct numerical and large eddy simulations of vertical pipe flows, *Phys. Fluids* **8**, 2590 (1996).
- [13] C. Marchioli, M. Picciotto, and A. Soldati, Influence of gravity and lift on particle velocity statistics and transfer rates in turbulent vertical channel flow, *Int. J. Multiphase Flow* **33**, 227 (2007).
- [14] C. Nilsen, H. I. Andersson, and L. Zhao, A Voronoi analysis of preferential concentration in a vertical channel flow, *Phys. Fluids* **25**, 115108 (2013).
- [15] J. L. Oliveira, C. W. Van Der Geld, and J. G. Kuerten, Concentration and velocity statistics of inertial particles in upward and downward pipe flow, *J. Fluid Mech.* **822**, 640 (2017).
- [16] K. O. Fong, O. Amili, and F. Coletti, Velocity and spatial distribution of inertial particles in a turbulent channel flow, *J. Fluid Mech.* **872**, 367 (2019).
- [17] S. Balachandar and J. K. Eaton, Turbulent dispersed multiphase flow, *Annu. Rev. Fluid Mech.* **42**, 111 (2010).
- [18] L. Brandt and F. Coletti, Particle-laden turbulence: Progress and perspectives, *Annu. Rev. Fluid Mech.* **54**, 159 (2022).
- [19] M. R. Maxey, The gravitational settling of aerosol particles in homogeneous turbulence and random flow fields, *J. Fluid Mech.* **174**, 441 (1987).
- [20] O. A. Druzhinin, Concentration waves and flow modification in a particle-laden circular vortex, *Phys. Fluids* **6**, 3276 (1994).
- [21] J. Ferry and S. Balachandar, A fast Eulerian method for disperse two-phase flow, *Int. J. Multiphase Flow* **27**, 1199 (2001).
- [22] J. Ferry, S. L. Rani, and S. Balachandar, A locally implicit improvement of the equilibrium Eulerian method, *Int. J. Multiphase Flow* **29**, 869 (2003).
- [23] O. A. Druzhinin and S. Elghobashi, Direct numerical simulations of bubble-laden turbulent flows using the two-fluid formulation, *Phys. Fluids* **10**, 685 (1998).
- [24] S. L. Rani and S. Balachandar, Evaluation of the equilibrium Eulerian approach for the evolution of particle concentration in isotropic turbulence, *Int. J. Multiphase Flow* **29**, 1793 (2003).
- [25] B. Shotorban and S. Balachandar, Particle concentration in homogeneous shear turbulence simulated via Lagrangian and equilibrium eulerian approaches, *Phys. Fluids* **18**, 065105 (2006).
- [26] M. Pilou, S. Tsangaris, P. Neofytou, C. Housiadas, and Y. Drossinos, Inertial particle deposition in a 90 laminar flow bend: An Eulerian fluid particle approach, *Aerosol Sci. Technol.* **45**, 1376 (2011).
- [27] M. Icardi, D. L. Marchisio, N. Chidambaram, and R. O. Fox, Equilibrium-eulerian les model for turbulent poly-dispersed particle-laden flow, *Int. J. Nonlinear Sci. Numer. Simul.* **14**, 139 (2013).
- [28] M. Cerminara, T. Esposti Ongaro, and L. C. Berselli, ASHEE-1.0: A compressible, equilibrium-Eulerian model for volcanic ash plumes, *Geosci. Model Dev.* **9**, 697 (2016).
- [29] D. Yang, B. Chen, S. A. Socolofsky, M. Chamecki, and C. Meneveau, Large-eddy simulation and parameterization of buoyant plume dynamics in stratified flow, *J. Fluid Mech.* **794**, 798 (2016).
- [30] A. K. Aiyer, D. Yang, M. Chamecki, and C. Meneveau, A population balance model for large eddy simulation of polydisperse droplet evolution, *J. Fluid Mech.* **878**, 700 (2019).
- [31] S. Balachandar, S. Zaleski, A. Soldati, G. Ahmadi, and L. Bourouiba, Host-to-host airborne transmission as a multiphase flow problem for science-based social distance guidelines, *Int. J. Multiph. Flow* **132**, 103439 (2020).
- [32] J. Borée, Extended proper orthogonal decomposition: A tool to analyse correlated events in turbulent flows, *Exp. Fluids* **35**, 188 (2003).
- [33] S. Maurel, J. Borée, and J. L. Lumley, Extended proper orthogonal decomposition: Application to jet/vortex interaction, flow, *Flow, Turbul. Combust.* **67**, 125 (2001).
- [34] C. Hoarau, J. Borée, J. Laumonier, and Y. Gervais, Analysis of the wall pressure trace downstream of a separated region using extended proper orthogonal decomposition, *Phys. Fluids* **18**, 055107 (2006).
- [35] A. Antoranz, A. Ianiro, O. Flores, and M. García-Villalba, Extended proper orthogonal decomposition of non-homogeneous thermal fields in a turbulent pipe flow, *Int. J. Heat Mass Transfer* **118**, 1264 (2018).
- [36] P. A. Kadu, Y. Sakai, Y. Ito, K. Iwano, M. Sugino, T. Katagiri, T. Hayase, and K. Nagata, Application of spectral proper orthogonal decomposition to velocity and passive scalar fields in a swirling coaxial jet, *Phys. Fluids* **32**, 015106 (2020).

- [37] K. Fukagata, K. Iwamoto, and N. Kasagi, Contribution of Reynolds stress distribution to the skin friction in wall-bounded flows, *Phys. Fluids* **14**, L73 (2002).
- [38] R. K. Schlander, S. Rigopoulos, and G. Papadakis, Analysis of wall mass transfer in turbulent pipe flow combining extended proper orthogonal decomposition and Fukugata-Iwamoto-Kasagi identity, *Phys. Rev. Fluids* **7**, 024603 (2022).
- [39] K. Fukagata, S. Zahrai, and F. H. Bark, Dynamics of Brownian particles in a turbulent channel flow, *Heat Mass Transfer* **40**, 715 (2004).
- [40] J. Ferry and S. Balachandar, Equilibrium expansion for the Eulerian velocity of small particles, *Powder Technol.* **125**, 131 (2002).
- [41] D. Richter and M. Chamecki, Inertial effects on the vertical transport of suspended particles in a turbulent boundary layer, *Bound.-Layer Meteorol.* **167**, 235 (2018).
- [42] H. Y. Tang, S. Rigopoulos, and G. Papadakis, On the interaction of turbulence with nucleation and growth in reaction crystallisation, *J. Fluid Mech.* **944**, A48 (2022).
- [43] G. El Khoury, P. Schlatter, A. Noorani, P. Fischer, G. Brethouwer, and A. Johansson, Direct numerical simulation of turbulent pipe flow at moderately high Reynolds numbers, *Flow, Turbul. Combust.* **91**, 475 (2013).
- [44] M. Veenman, Ph.D. thesis, Eindhoven University of Technology, 2004.
- [45] M. Elimelech, J. Gregory, X. Jia, and R. Williams, *Particle Deposition and Aggregation; Measurement, Modeling and Simulation*, 1st ed. (Butterworth-Heinemann, Burlington, 1995), Vol. 125.
- [46] K. Mikhaylov, S. Rigopoulos, and G. Papadakis, Reconstruction of large-scale flow structures in a stirred tank from limited sensor data, *AIChE J.* **67**e17348 (2021).
- [47] H. Yao and G. Papadakis, On the role of the laminar/turbulent interface in energy transfer between scales in bypass transition, *J. Fluid Mech.* **960**, A24 (2023).
- [48] H. Yao, J.-P. Mollicone, and G. Papadakis, Analysis of interscale energy transfer in a boundary layer undergoing bypass transition, *J. Fluid Mech.* **941**, A14 (2022).
- [49] S. Lu and G. Papadakis, Flow reconstruction around a surface-mounted prism from sparse velocity and/or scalar measurements using a combination of pod and a data-driven estimator, *Flow, Turbul. Combust.* **110**, 1059 (2023).
- [50] S. Balay, S. Abhyankar, M. F. Adams, S. Benson, J. Brown, P. Brune, K. Buschelman, E. Constantinescu, L. Dalcin, A. Dener, V. Eijkhout, J. Faibussowitsch, W. D. Gropp, V. Hapla, T. Isaac, P. Jolivet, D. Karpeev, D. Kaushik, M. G. Knepley, F. Kong, S. Kruger, D. A. May, L. C. McInnes, R. T. Mills, L. Mitchell, T. Munson, J. E. Roman, K. Rupp, P. Sanan, J. Sarich, B. F. Smith, S. Zampini, H. Zhang, H. Zhang, and J. Zhang, PETSc/TAO users manual, Tech. Rep. ANL-21/39 - Revision 3.18, Argonne National Laboratory (2022).
- [51] R. D. Falgout and U. M. Yang, Hypre: A library of high performance preconditioners, in *Computational Science — ICCS 2002*, edited by P. M. A. Sloot, A. G. Hoekstra, C. J. K. Tan, and J. J. Dongarra (Springer, Berlin, Heidelberg, 2002), pp. 632–641.
- [52] X. Wu and P. Moin, A direct numerical simulation study on the mean velocity characteristics in turbulent pipe flow, *J. Fluid Mech.* **608**, 81 (2008).
- [53] S. B. Pope, *Turbulent Flows*, 1st ed. (Cambridge University Press, 2000).
- [54] J. L. Lumley, Atmospheric Turbulence and Radio Wave Propagation, in *Proceedings of the international Colloquium Moscow* (1965), pp. 166–176.
- [55] F. Picano, G. Sardina, and C. M. Casciola, Spatial development of particle-laden turbulent pipe flow, *Phys. Fluids* **21**, 093305 (2009).
- [56] G. Sardina, F. Picano, P. Schlatter, L. Brandt, and C. M. Casciola, Large scale accumulation patterns of inertial particles in wall-bounded turbulent flow, *Flow, Turbul. Combust.* **86**, 519 (2011).
- [57] J. Lee, S. Y. Jung, H. J. Sung, and T. A. Zaki, Turbulent thermal boundary layers with temperature-dependent viscosity, *Int. J. Heat Fluid Flow* **49**, 43 (2014).
- [58] H. Nemati, A. Patel, B. J. Boersma, and R. Pecnik, The effect of thermal boundary conditions on forced convection heat transfer to fluids at supercritical pressure, *J. Fluid Mech.* **800**, 531 (2016).
- [59] S. Pandey, X. Chu, E. Laurien, and B. Weigand, Buoyancy induced turbulence modulation in pipe flow at supercritical pressure under cooling conditions, *Phys. Fluids* **30**, 065105 (2018).

- [60] J. Capecelatro and O. Desjardins, Mass loading effects on turbulence modulation by particle clustering in dilute and moderately dilute channel flows, *J. Fluids Eng.* **137**, 111102 (2015).
- [61] J. Eaton and J. Fessler, Preferential concentration of particles by turbulence, *Int. J. Multiphase Flow* **20**, 169 (1994).
- [62] H. Abe and R. A. Antonia, Near-wall similarity between velocity and scalar fluctuations in a turbulent channel flow, *Phys. Fluids* **21**, 025109 (2009).
- [63] R. A. Antonia, H. Abe, and H. Kawamura, Analogy between velocity and scalar fields in a turbulent channel flow, *J. Fluid Mech.* **628**, 241 (2009).
- [64] A. Dugdale, K. S. Ball, M. R. Paul, and P. F. Fischer, Dynamical eigenfunction decomposition of turbulent pipe flow, *J. Turbul.* **8**, N43 (2007).
- [65] I. Marusic, D. Chandran, A. Rouhi, M. K. Fu, D. Wine, B. Holloway, D. Chung, and A. J. Smits, An energy-efficient pathway to turbulent drag reduction, *Nat. Commun.* **12**, 5805 (2021).
- [66] N. Kasagi, Y. Hasegawa, K. Fukagata, and K. Iwamoto, Control of turbulent transport: Less friction and more heat transfer, *J. Heat Transfer* **134**, 031009 (2012).
- [67] [www.ukturbulence.co.uk](http://www.ukturbulence.co.uk)